# MOUNTAIN-PLAINS CONSORTIUM

**MPC 22-473** | C. Pantelides and S. Neupane

## ANALYSIS OF ABC BRIDGE COLUMN-TO-FOOTING JOINTS WITH RECESSED SPLICE SLEEVE CONNECTORS

MOUNTAIN-PLAINS CONSORTIUM REGION 8

A University Transportation Center sponsored by the U.S. Department of Transportation serving the Mountain-Plains Region. Consortium members:

Colorado State University
North Dakota State University
South Dakota State University
University of Colorado Denver
University of Denver
University of Utah
Utah State University
University of Wyoming

**Technical Report Documentation Page**

| 1. Report No. | 2. Government Accession No. | 3. Recipient's Catalog No. |
|---|---|---|
| MPC-638 | | |

| 4. Title and Subtitle | 5. Report Date |
|---|---|
| Analysis of ABC Bridge Column-to-Footing Joints with Recessed Splice Sleeve Connectors | July 2022 |
| | 6. Performing Organization Code |

| 7. Author(s) | 8. Performing Organization Report No. |
|---|---|
| C. Pantelides<br>S. Neupane | MPC 22-473 |

| 9. Performing Organization Name and Address | 10. Work Unit No. (TRAIS) |
|---|---|
| University of Utah<br>Department of Civil and Environmental Engineering<br>110 Central Campus Drive<br>Room 2115<br>Salt Lake City, UT 84112 | 11. Contract or Grant No. |

| 12. Sponsoring Agency Name and Address | 13. Type of Report and Period Covered |
|---|---|
| Mountain-Plains Consortium<br>North Dakota State University<br>PO Box 6050, Fargo, ND 58108 | Final Report |
| | 14. Sponsoring Agency Code |

15. Supplementary Notes

Supported by a grant from the US DOT, University Transportation Centers Program

16. Abstract

The use of precast concrete in bridge construction has been abundant in recent years because of its efficiency and superior quality control. Precast components are connected at the bridge site to reduce construction time and traffic disturbance. The Grouted Splice Sleeve (GSS) connection provides good bending moment resistance between precast reinforced concrete (RC) components. This connection type has been widely employed in non-seismic areas. The use of this connection in moderate or high seismic zones has been explored and proposed for medium-size highway bridges. It is essential to propose a numerical modeling technique at the local and global level with the proposed connection type. The primary goal of this project is to compare the computational model to experimental results under cyclic quasi-static loading; the computational model is then used to generate the structural response of a bridge bent under seismic loading. Using existing material models and a forced-based beam-column fiber element that accounts for fatigue, bar-slip, purposeful debonding, and plastic hinge length, a computer model capable of predicting structural response under cyclic loading is constructed. The computational model is subsequently utilized to calculate the seismic response of a three-column bridge bent to near-field and far-field earthquakes in terms of overall maximum drift ratio and drift ratio at the maximum level of seismic demand.

| 17. Key Word | 18. Distribution Statement |
|---|---|
| bridge construction, columns, earthquake resistant design, footings, joints (engineering), precast concrete | Public distribution |

| 19. Security Classif. (of this report) | 20. Security Classif. (of this page) | 21. No. of Pages | 22. Price |
|---|---|---|---|
| Unclassified | Unclassified | 52 | n/a |

# Analysis of ABC Bridge Column-to-Footing Joints with Recessed Splice Sleeve Connectors

Chris P. Pantelides
Professor

Suman Neupane
Graduate Student

Department of Civil and Environmental Engineering
The University of Utah

July 2022

## Acknowledgments

The authors acknowledge the financial support provided by the Mountain-Plains Consortium (MPC) under project MPC-638.

## Disclaimer

The contents of this report reflect the views of the authors, who are responsible for the facts and the accuracy of the information presented. This document is disseminated under the sponsorship of the Department of Transportation, University Transportation Centers Program, in the interest of information exchange. The U.S. Government assumes no liability for the contents or use thereof.

# ABSTRACT

The use of precast concrete in bridge construction has been abundant in recent years because of its efficiency and superior quality control. Precast components are connected at the bridge site to reduce construction time and traffic disturbance. The Grouted Splice Sleeve (GSS) connection provides good bending moment resistance between precast reinforced concrete (RC) components. This connection type has been widely employed in non-seismic areas. The use of this connection in moderate or high seismic zones has been explored and proposed for medium-size highway bridges. It is essential to propose a numerical modeling technique at the local and global level with the proposed connection type. The primary goal of this project is to compare the computational model to experimental results under cyclic quasi-static loading; the computational model is then used to generate the structural response of a bridge bent under seismic loading. Using existing material models and a forced-based beam-column fiber element that accounts for fatigue, bar-slip, purposeful debonding, and plastic hinge length, a computer model capable of predicting structural response under cyclic loading is constructed. The computational model is subsequently utilized to calculate the seismic response of a three-column bridge bent to near-field and far-field earthquakes in terms of overall maximum drift ratio and drift ratio at the maximum level of seismic demand.

# TABLE OF CONTENTS

# LIST OF FIGURES

# LIST OF TABLES

# EXECUTIVE SUMMARY

This research proposes a computational modeling technique that can predict the local and global response of column-to-footing joints with recessed grouted spliced sleeves (GSS) and intentional debonding. The model is focused on the local response of the GSS and the load path within the connection; in addition, the bond-slip response of the GSS is characterized. When intentional debonding is present, the contribution of reinforcing bars to structural response is softened, and a new model is needed that includes this effect; intentional debonding changes the extent of the strain penetration region resulting in a different plastic hinge length. Hysteretic energy from loading cycles is compared to verify the agreement of the proposed numerical model with experimental results. Several modeling considerations are used, including plastic hinge length, bond-slip, debonding behavior, and low-cycle fatigue to match the experimental behavior of the columns tested under cyclic loading. The numerical model was prepared, and numerical results were obtained regarding local and global response of the Cast-in-Place (CIP) column-to-footing connection, and Test 1 and Test 2 type column-to-footing connections with intentional debonding. Results showed that the hysteretic response obtained due to cyclic loading was almost identical for the proposed numerical model and the experimental results. The cumulative error in hysteretic energy was found to be 6% and 2% respectively for the Test 1 and Test 2 type specimens. The experiments were stopped when fracture of a longitudinal bar occurred or when there was a 20% drop in the peak load during cyclic loading. After validating the computational model using the experiments carried out by Ameli et al. (2016) and Barton et al. (2022), a three-column bridge bent from an actual bridge was modeled, including Soil Structure Interaction (SSI); the results of the model were compared with the full-scale experiment of a three-column bridge bent carried out by (Pantelides et al. 2004). The seismic response of the proposed three-column bridge bent was investigated under far-field and near-field ground motions and the performance was evaluated using the demand-capacity ratio at maximum drift and the drift ratio at maximum seismic demand.

# LIST OF ACRONYMS

| | |
|---|---|
| **AASHTO** | American Association of State Highway and Transportation Officials |
| **ABC** | Accelerated Bridge Construction |
| **ACI** | American Concrete Institute |
| **ASTM** | American Society of Testing and Materials |
| **FHWA** | Federal Highway Administration |
| **SSI** | Soil Structure Interaction |
| **GSS** | Grouted Splice Sleeve Connectors |
| **CIP** | Cast in Place |
| **PCB** | Precast Bridge Bent |
| **LVDT** | Linear Variable Differential Transducer |
| **OpenSeeS** | Open System for Earthquake Engineering Simulation |
| **UDOT** | Utah Department of Transportation |

# 1. INTRODUCTION

The bridge construction technique used to decrease delays due to traffic and weather-related issues and for which the structural components are prefabricated off-site and then transported to the bridge site for installation is termed Accelerated Bridge Construction, or ABC. The typical column is connected to a spread footing or cap beam at the interface with bars grouted in ducts or grouted splice sleeves (GSS). The use of GSS saves time and reduces traffic and delays during bridge construction (Ameli et al. 2015, 2016; Haber et al. 2014). Bridge designers must design the bridge so the ABC method can meet or exceed the performance of the bridge using the Cast-in-Place (CIP) construction method. This research aims to show the ABC concept and implementation and present the numerical model developed for bridges in high seismic zones. Bond-slip controls the progression of damage during cyclic loading in the structure. As a result, further study into the bond-slip process is necessary to properly model the performance of the structure. Bond-slip is confirmed as one of the principal sources of structural damage; intentional debonding is implemented to prolong the occurrence of failure in earthquake-prone regions (Melo et al. 2011).

High-strength grout filled splice sleeves (GSS) are used to connect several pairs of reinforcing bars, one from the column and one from the footing, in each GSS connector. GSS are employed in precast construction because they limit damage to a concentrated area and offer the benefits of ABC (Ameli et al. 2015, 2016; Haber et al. 2014). When exposed to cyclic loading, a half-scale column-to-footing joint with a recessed spliced sleeve was examined and modeled. The researchers used grouted splice sleeves to anchor dowels from the footing and longitudinal reinforcing bars from the column. It has been found that the splice sleeve location is critical for good performance during seismic loading. AASTHO LFRD bridge design specification (2012) suggests that reinforcing bars should be either lap spliced, welded, or used with a mechanical connection system for better performance. Mechanical connections are acceptable if they can generate a yield strength of 125% of the specified yield strength as suggested by AASTHO guidelines.

The column-to-footing connection using GSS was studied in this report. This report is concerned with the response of a bridge system when GSS are recessed below the column-to-footing interface. The performance of the bridge in seismic zones is greatly influenced by the connection between the precast components. Numerous studies are now being conducted to investigate various connection details, their efficacy, and their usability. Three important acceptance requirements for any bridge located in a seismic area are ductility, reparability, and lateral load capability (Ameli 2016).

## 1.1 Common ABC Connections in Seismic Zones

While constructing ABC bridges it is essential to use a connection type efficiently, so the performance of the joints is not compromised during any seismic event. In general construction practice, the following connection types are used: grouted splice sleeves, grouted duct, pocket and socket connection, and the use of post-tensioning bars as connectors.

### 1.1.1 Grouted Duct Connection

The column steel reinforcement projects from the column into steel corrugated pipes inside the cap-beam or footing and is connected using high-strength grout in grouted duct type connections. During the previous study by Raynor et al. (2002) it was seen that the bond-slip behavior of the reinforcing bar inside the grouted duct has some effect on structural performance. The use of ducts contributes toward the bond-slip effect and causes failure in grouted duct connection regions (Brenes et al. 2006). Anchorage of a length equal to 6 to 10 times the bar diameter is essential for good performance as suggested by (Steuck et

al. 2009). Recently, use of ultra-high performance concrete was shown to improve the performance of system; this not only makes the response comparable to the cast-in-place specimen but can improve the performance in terms of displacement and energy dissipation capacity (Tazarv and Saiidi 2015).

### 1.1.2 Pocket Connection

The connection technique in which reinforcing bars are placed in the pocket of space formed by using a circular corrugated steel duct is known as pocket connection. In this type of connection, the pocket space — once the column reinforcing bar is inserted — is filled with normal concrete. This type of connection demands higher embedment length than that of other connection types. In one of the tests performed, using two column bridge bents reduced to 40% scale, it was found that the embedment length should be equal to 1.5 times the column diameter (Motaref et al. 2011).

### 1.1.3 Socket Connection

A precast column and the protruded reinforcing bars are connected to a spread footing, whereby the footing is prepared around projected reinforcing bars from the footing, is known as the socket connection. The performance of the socket connection was evaluated by Khaleghi et al. (2012); they found that the reduced-scaled specimen performed better than that of a monolithic specimen, showing the possibility of using this type of connection in seismic regions. Since reinforcing projected from the precast column are concreted together with the spread footing, failure mechanisms matched the cast-in-place specimen (Wang et al. 2019). The performance evaluation of such type of socket connection shows that the column can achieve ultimate lateral drifts of more than 6%, which is higher than the recommended value in design specifications, suggesting that such a type of connection can be used effectively in seismically active regions.

### 1.1.4 Post-tensioning System

Post-tensioning bars can be used as the connectors between the column and footing interface and with energy dissipators, such as buckling restrained braces (BRB's), viscous dampers, shape memory alloys, energy dissipating mechanical devices and stretch length anchors (SLA) (Lee and Billington 2009). Post-tensioning elements only pass through the column to footing/cap-beam interface; no reinforcing bars from the column pass through the footing/cap-beam and vice versa. Use of post-tensioning bars produces rocking behavior, reducing the permanent lateral deformation of the system. This type of connection has been popular in recent years because of its self-centering capabilities.

### 1.1.5 Grouted Spliced Sleeves (GSS)

GSS connection is one type of connection used in accelerated bridge construction. In a GSS type connection, grouted splice sleeves are used as the connector to connect factory with field dowels. GSS can be used in two ways, one in which the field bar is grouted in one end and the factory bar is fastened to another end, known as Fastened Grouted Spliced Sleeve (FGSS) and another method where both field and factory bars are grouted on both ends known as Grouted-Grouted Spliced Sleeve (GGSS). Throughout this research, GGSS connectors were used; these connectors are recessed below the column-to-footing interface, well within the footing. Bond stress developed between the reinforcing bars and the high strength grout helps in transferring the compressive and tensile forces induced during cyclic loading. Reinforcing bars used in GGSS require low embedment length (25% percent of the embedment length prescribed by specifications) because these bars develop sufficient strength due to the presence of high confinement. The high level of confinement helps in preventing splitting failure. Figure 1.1 shows typical GSS connections.

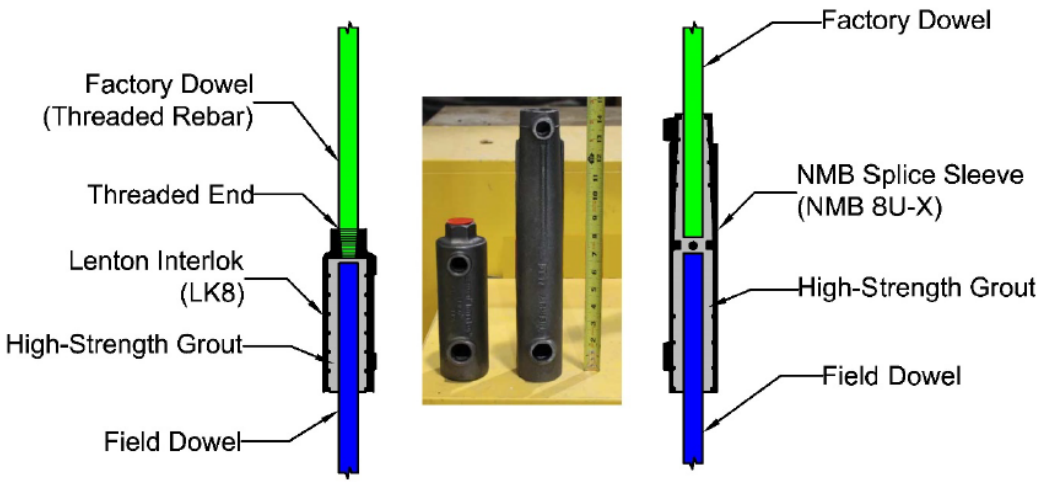


**Figure 1.1** Two types of grouted splice sleeve connectors used in this research: FGSS on the left and GGSS on the right

# 2. DESIGN AND CONSTRUCTION OF BRIDGE BENT

Two column-to-footing specimens were tested by Barton et al. (2022); the specimens had similar dimensions as those tested by Ameli et al. (2017), so the results can be compared. These specimens were prepared in such a way that they were a half-scaled specimen of the actual bridge. The specimens prepared by Barton et al. (2022) had intentional debonding and recessed spliced sleeves as the parameters of interest. Both specimens had spliced sleeve connectors recessed below the column-to-footing interface. The spliced sleeves were recessed 8 bar diameters ($8d_b$) below the column-to-footing interface in both specimens. NMB spliced sleeves were used for the study, and the connection between factory and field dowel was designed as grouted on both sides. The only difference between the two specimens was the amount of intentional debonding inside the footing.

The column cross-section and details of intentional debonding are shown in Figure 2.1. The reinforcing bars extended from the column were intentionally debonded before they were grouted in spliced sleeves. The length of intentional debonding ($DL$) was 8 bar diameters ($8d_b$) for the case of Test 1 specimen, which was performed completely inside the footing surface. In the case of Test 2 specimen, the length of intentional debonding was distributed equally in the column and footing; a length of four bar diameters ($4d_b$) was intentionally debonded in the column and the remaining length of four bar diameters ($4d_b$) was intentionally debonded inside footing. Since the GSS was recessed 8 bar diameters ($8d_b$) below the column-to-footing interface, the remaining length of 4 bar diameters ($4d_b$) was bonded with the footing concrete for the Test 2 specimen. Each column had six #8 bars for longitudinal reinforcement that were confined using #4 spirals spaced at 2.5 in. on center.

The number and size of reinforcing bars used in both tests were identical to those used by Ameli et al. (2017). Intentional debonding was carried out, since it allows a better strain distribution in the reinforcing bars and it postpones bar fracture due to low cycle fatigue. In general practice, duct tape is wrapped around the reinforcing bar for debonding, but this test included the use of PVC pipe around the reinforcing bars. The use of PVC pipe allowed debonding against friction and chemical interaction, whereas the conventional method of duct taping is only able to break the chemical interaction between concrete and reinforcing bar. The intentionally debonded columns are subsequently grouted using spliced sleeves. Grout was prepared and poured into the ducts and tamped to remove air pockets. Concrete compressive strength after 28 days was measured and found to be 10.7 ksi; the grout strength was found to be 15.1 ksi for Test 1 and 16.3 ksi for Test 2.

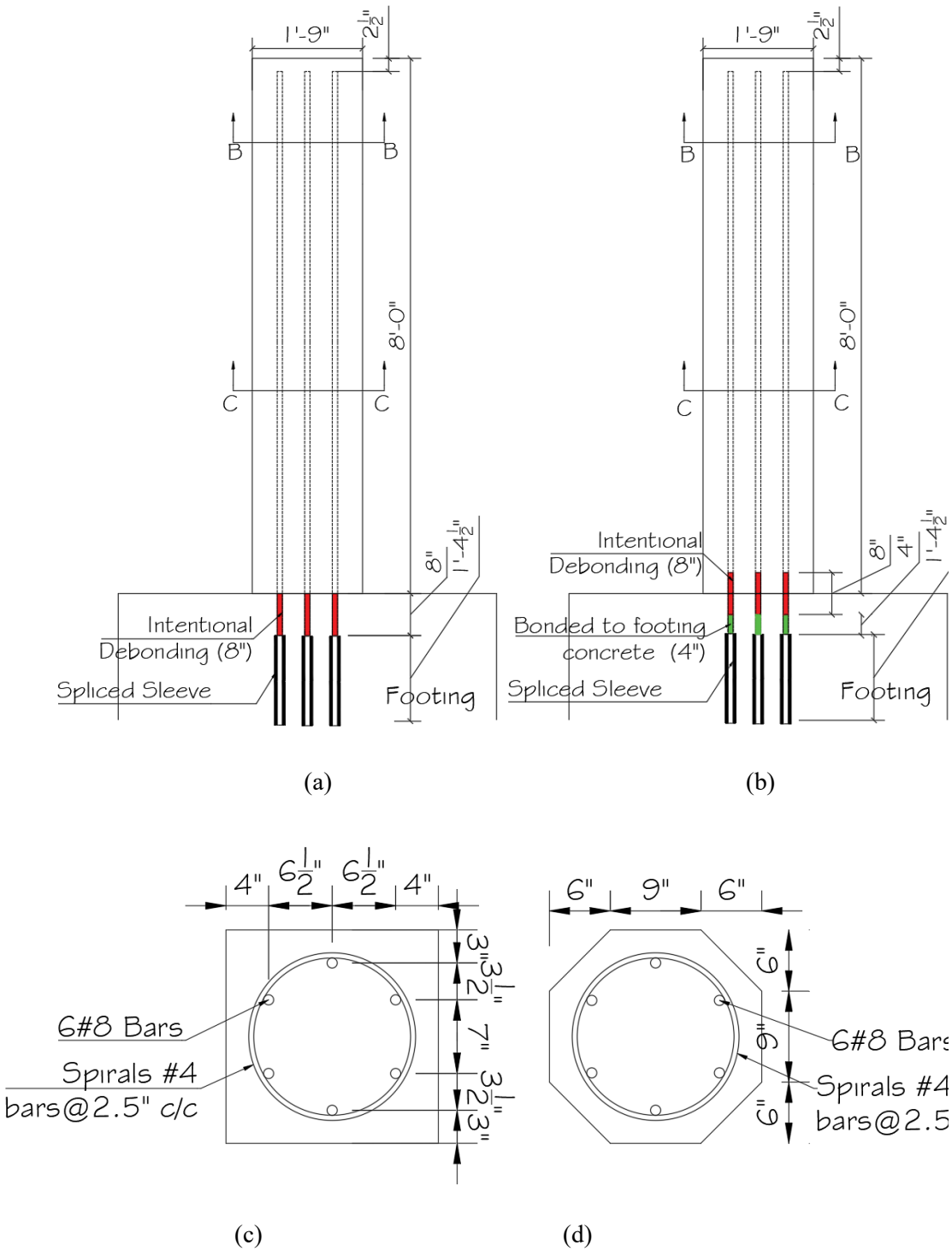


**Figure 2.1** Column Details: (a) Test 1 column; (b) Test 2 column; (c) cross-section of column at B-B, and (d) cross-section of column at C-C

# 3. TEST SETUP AND RESULTS

## 3.1 Test Setup

The cantilever column was connected to the footing, which was fixed at the base with the strong floor of the Structures Laboratory at the University of Utah. Threaded bars were used to fix the footing to the strong floor using wide flange steel I-beams. A hydraulic actuator was used to apply the cyclic quasi-static cyclic load at the top of the column. Axial load was applied by using a hydraulic system and threaded bars, fixed at the top of the column and the bottom of the footing. The lateral cyclic load was applied on the square face section at a height of 8 ft – 0 in. from the column-to-footing interface, using displacement control. Strain gauges were provided to measure strain in the reinforcing bars during cyclic loading, string pots were used to measure the lateral displacement of the column, and Linear Variable Displacement Transducers (LVDTs) were used to measure column rotation and curvature at several locations. The typical setup of the experimental study is shown in Figure 3.1(a).

Cyclic load was applied using the actuator at the top of the column. The applied cyclic load was displacement-controlled consisting of two push and pull cycles. The experiment was run at two different displacement rates: up to 3% drift ratio, the displacement rate was 1.2 in./min, which was increased above the 3% drift ratio to 4.0 in./min. The cyclic loading protocol is shown in Figure 3.1(b).

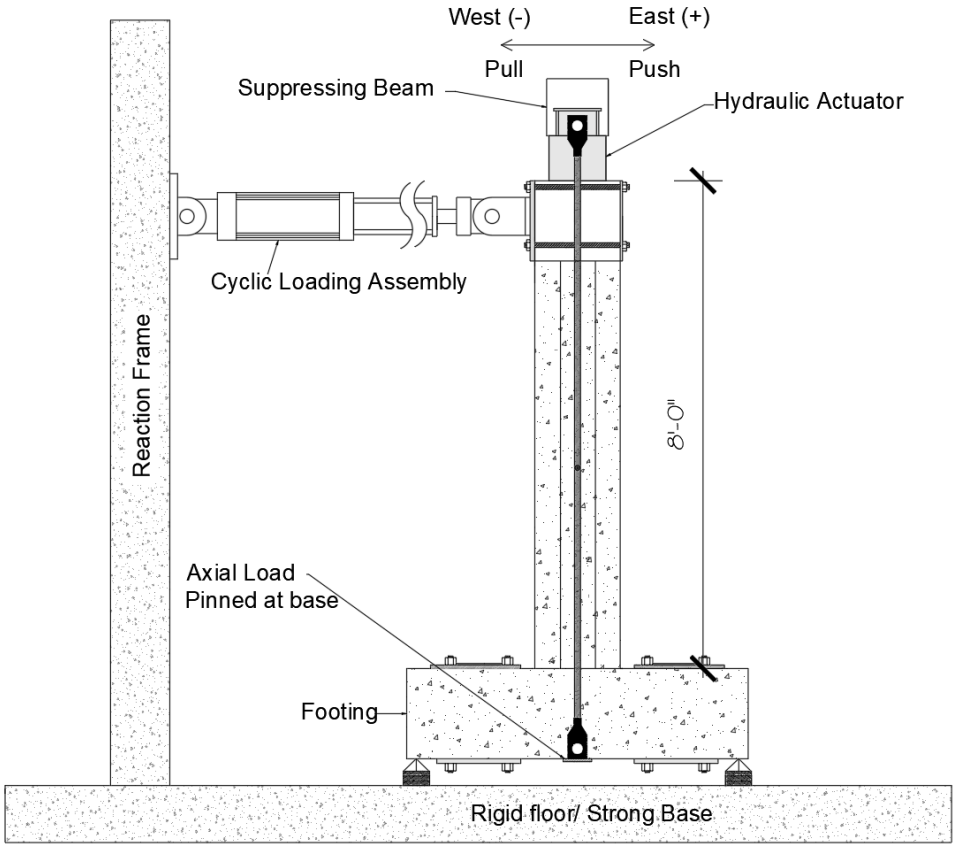


**(a)**

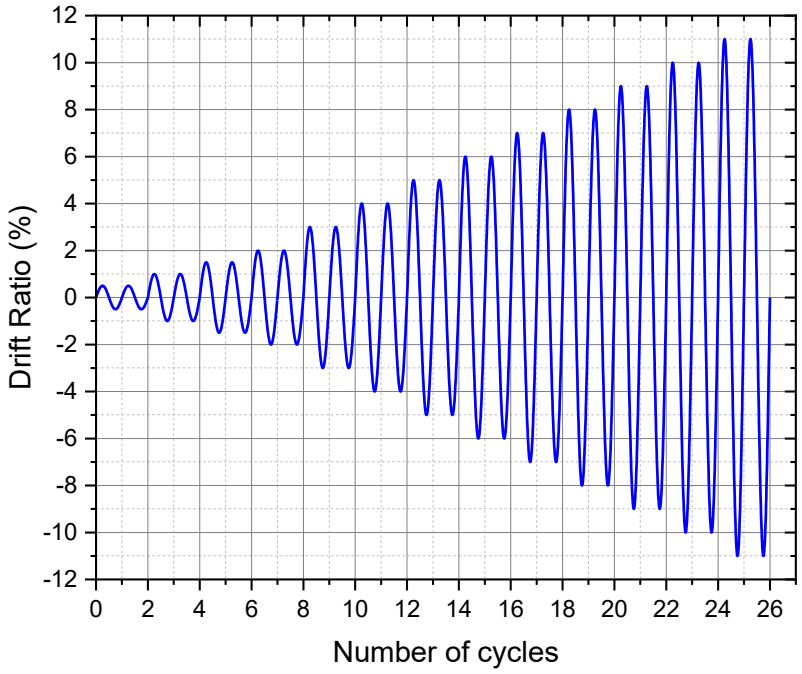


**(b)**

**Figure 3.1** Test setup: (a) experimental setup; (b) cyclic loading protocol

## 3.2 Test Results

Application of cyclic load on Test 1 and Test 2 specimens, resulted in force vs. displacement hysteretic curves, strains, and hysteretic energy dissipation. Based on these results, ductility, bar fracture, concrete cracking, and concrete spalling were studied. The results obtained were compared with the CIP monolithic specimen to verify the performance of the proposed specimens during cyclic lateral loading.

**Test 1**

The hysteretic response showed wide hysteretic loops, suggesting that Test 1 type of arrangement dissipates higher energy than that the other specimens tested; there was no significant drop in strength until the specimen reached an 11% drift ratio, after which fracture of a reinforcing bar in the column occurred and a drop in strength was observed. The test was terminated at this drift ratio since the drop in lateral load was 20 % of the maximum. The hysteretic performance showed that the maximum lateral load that the specimen achieved was 37.9 kip. Figure 3.2 shows the hysteretic loops from the experiment for Test 1 specimen. The total cumulative hysteretic energy was found to be 5,115 in.-kip for Test 1 specimen.

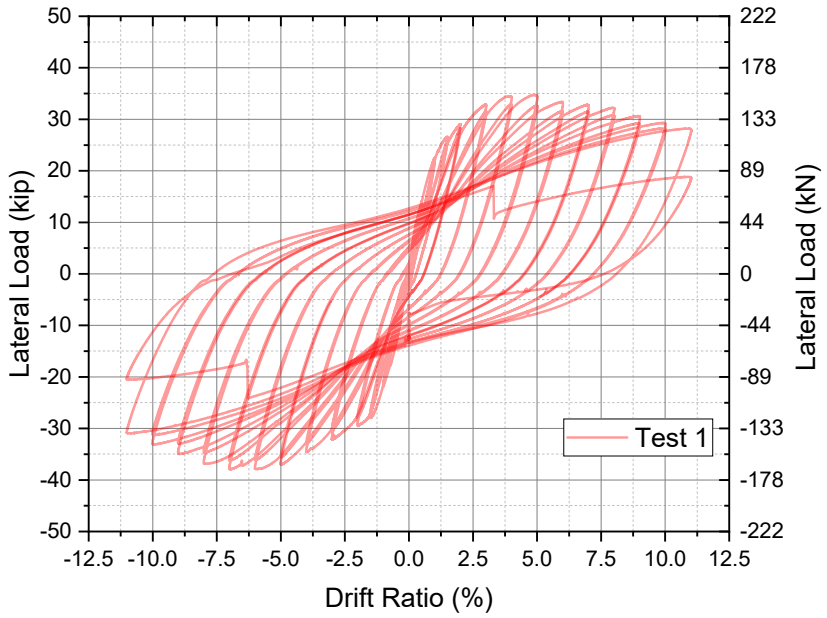


**Figure 3.2** Hysteretic performance of Test 1 specimen

**Test 2**

In the Test 2 specimen, intentional debonding was distributed equally in the column and the footing. The hysteretic loops were narrow compared to the Test 1 specimen, which suggests that the hysteretic energy dissipated was lower than the Test 1 specimen. Reinforcing bar fracture occurred at the 9% drift ratio. The hysteretic performance showed that the maximum lateral load that the specimen achieved was 41.1 kip. Figure 3.3 shows the hysteretic loops from the experiment for Test 2 specimen. The hysteretic energy for this case was found to be 3,506 in.-kip, which is lower than that of Test 1 specimen.

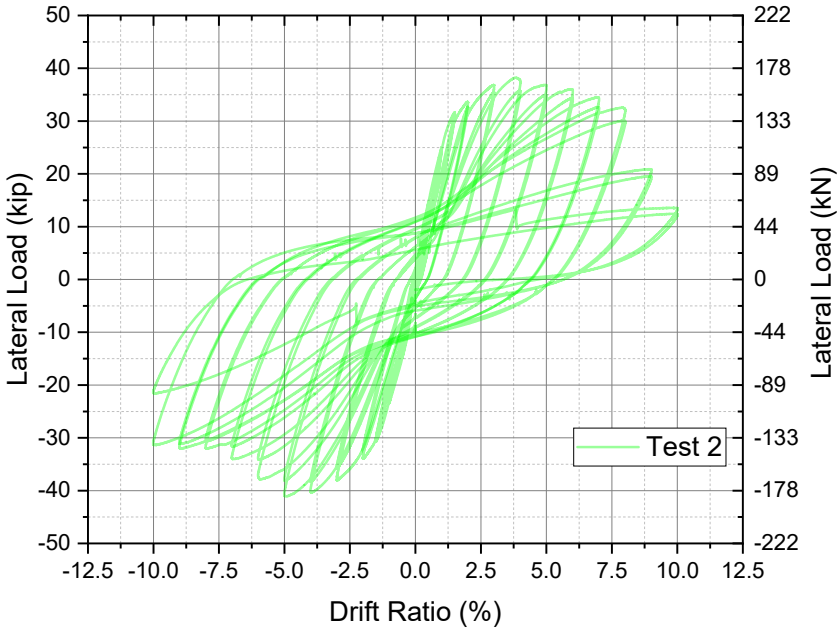


**Figure 3.3** Hysteretic performance of Test 2 specimen

**Comparison between monolithic (CIP), Test 1, and Test 2 Specimens**

Once the experimental results were found, they were compared with the experimental results of the monolithic (CIP) specimen, tested by Ameli et al. (2017). The Test 1 specimen almost had 1.5 times higher hysteretic energy dissipation than that the CIP and Test 2. Both Test 2 and CIP reached 9% drift ratio before failure whereas Test 1 had a higher drift capacity of 11% before failure. Figure 3.4 shows the hysteretic plots for Test 1, Test 2 and CIP specimens. Table 3.1 shows the summary of experimental results obtained.

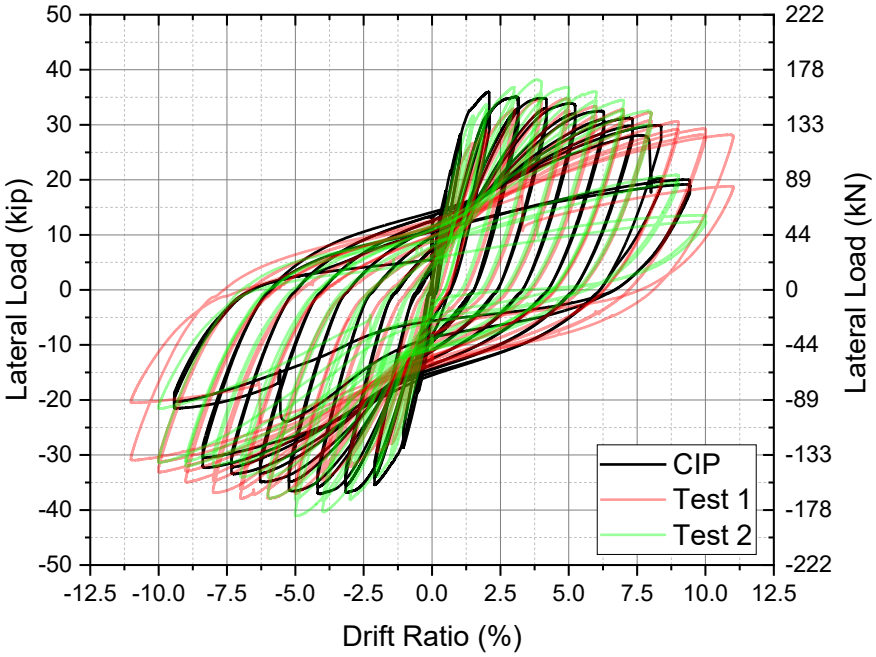


**Figure 3.4** Hysteretic performance of Test 1, Test 2 and CIP specimen

**Table 3.1** Summary of experimental results

| Parameters | Test 1 | Test 2 | CIP |
|---|---|---|---|
| Drift ratio at failure (%) | 11 | 9 | 9 |
| Initial stiffness (kip/in.) | 22.11 | 24.44 | 35.84 |
| Ductility | 7.5 | 5.4 | 9.9 |
| Hysteretic energy (in.-kip) | 5,115 | 3,506 | 3,906 |

# 4. NUMERICAL MODEL

## 4.1 Numerical Modeling

It is crucial to develop an appropriate model that can predict material behavior as a result of intentional debonding; current modeling methodologies do not handle the effect of intentional debonding efficiently. A distributed plasticity model is employed because non-linear behavior during the application of lateral loads may occur in any region of a structural member. A discretized fiber element model based on stress-strain relationships for uniaxial materials is developed. Global response is calculated by numerical integration and discretization of fibers into several components. Investigations into various component failures are carried out as a local response parameter. To represent structural behavior, a comprehensive numerical model that can simulate structural action during an earthquake is needed. We focus on the numerical model and its ability to predict the response of the two specimens loaded with quasi-static cyclic loads. An open-source finite element software framework OpenSees (McKenna et al. 2010) will be used to simulate the effects on the specimens during cyclic loading that will be further expanded for an actual bridge bent under earthquake excitations.

## 4.2 Previous Modeling Efforts

To determine whether alternative designs for seismic resisting components are practical, physical tests are necessary. However, to use these alternative designs, it is crucial to be able to build a numerical model that accurately depicts the specimens tested. In this way, the components can be used without having to perform tests for every scenario. A numerical model that will make it possible to represent accurately the behavior of the columns has been developed utilizing several analytical models. The ability of the spliced reinforcing bar to deform is controlled using mechanical splice sleeves. The moment-rotation capability of the structure is significantly impacted by the employment of spliced sleeves and their physical characteristics, frequently resulting in a reduction in deformation capacity (Haber et al. 2015).

Spliced sleeves, when used in structures, affect the uniaxial stress behavior; it is essential to find the exact uniaxial stress-strain behavior developed in the spliced sleeve to develop a good numerical model. Uniaxial material properties were studied, which can be utilized in plastic hinge regions (Dahal et al. 2019; Haber et al. 2015). Performance of the structure is assessed by using its response in terms of strength and displacement ductility characteristics. When the structure with GSS connections performs similarly to a monolithic structure, the GSS connection is deemed acceptable (Pang et al. 2010; Tazarv and Saiidi 2016). Precast sub-assemblies are anticipated to have an equivalent strength capacity to the monolithic sub-assembly to replicate the performance of monolithic structures. Numerical studies show that debonding of steel reinforcing bars outside of the GSS connections can increase displacement capacity (Ameli et al. 2016; Tazarv and Saiidi 2014).

The 3D finite element numerical model suggested by (Sideris 2012) was capable of reproducing the response of hybrid rocking bridge piers with varied connection. This numerical model could predict the performance of bridge piers under a cyclic quasi-static loading and the results were verified with the experimental outcomes. This verified numerical finite element model was further used for parametric studies. Tazarv and Saiidi (2014) studied the use of a grouted duct on a column-to-footing connection accounting for bond-slip behavior; they developed a 2D model that could predict behavior under seismic motions and quasi-static cyclic loading when Ultra-High-Performance Concrete (UHPC) is used in a duct Tazarv and Saiidi (2015). Similarly, Ameli et al. (2016) developed a numerical model using 1D springs to obtain the modified reinforcing bar properties when the bond between reinforcing bar and grout slips causing changes in strain. To replicate bond-slip performance, the *force-based beamcolumn* element is used to model flexural response and non-linear behavior. This *force-based beamcolumn* element allows

one to simulate material behavior in the plastic hinge region. Bond-slip is modeled using equivalent material characteristics (Dahal et al. 2019; Haber 2013).

Zhao and Sritharan (2007) developed a numerical relation for the strain penetration behavior in reinforcing bars due to bond-slip between the reinforcing bar and concrete. They used a zero-length spring element having properties obtained from the constitutive model for bond-slip effects. The experimental and numerical study by Zhao and Sritharan (2007) showed better agreement compared to results obtained from numerical models, which did not include the strain-penetration effect due to bond-slip. Intentional debonding is performed in the plastic hinge region so that failure of the reinforcing bars can be delayed by reducing the effect of low cycle fatigue. Numerically modelling the effect of intentional debonding is relatively new. Tazarv and Saiidi (2015) have proposed a numerical model, which can be used to obtain the effect of intentional debonding in terms of modified material properties in the plastic hinge region.

## 4.3 Material Model

### 4.3.1 Concrete

Different material properties can be obtained for the core and cover concrete through the use of Mander's model (Mander et al. 1988). The cover concrete is designed as an unconfined concrete to simulate the cylinder concrete compression testing. Similarly, the core concrete is classified as confined concrete and represented with the hoops providing confining pressure. Both confined and unconfined concrete are modeled as *uniaxialMaterial Concrete04 (Popovic Concrete Material). Concrete04* Material is basically defined by four parameters: the 28-day compressive strength of concrete ($f_c$'), the concrete strain at maximum strength ($\varepsilon_{cc}$), the concrete strain at crushing strain ($\varepsilon_{cu}$), and the initial stiffness of the stress-strain curve ($E_c$). Figure 4.1 shows the detailed stress-strain curve used to model concrete using Mander's model for both confined core concrete and unconfined cover concrete.

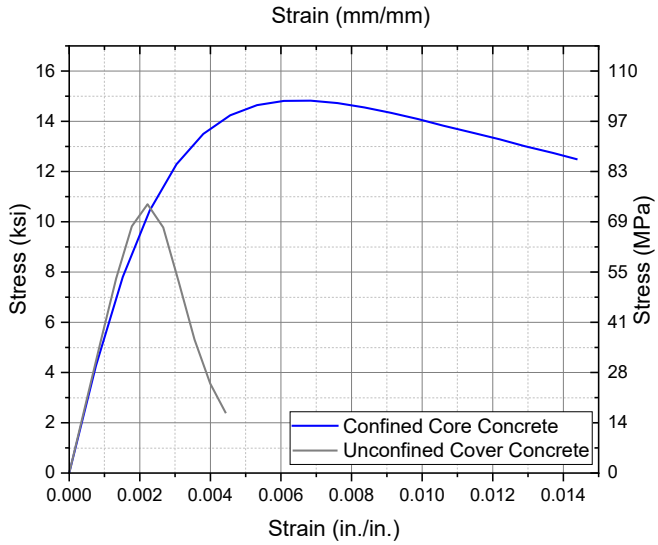


**Figure 4.1** Concrete material model (Mander et al. 1988)

### 4.3.2 Mild Steel Reinforcing Bar

Reinforcing bars were modeled using *ReinforcingSteel* material available in OpenSees (Kunnath et al. 2009). This uniaxial material incorporated reinforcing bar properties, including stress-strain performance of reinforcing bars under lateral load. The reinforcing steel was modeled as an isotropic strain-hardening material, including yield strength, ultimate strength, modulus of elasticity, tangent modulus of elasticity at initial strain hardening, and strain corresponding to hardening of the steel reinforcing bar. Fatigue parameters are based on the Coffin-Manson equation Manson (1965). The reinforcing bar buckling model was based on Dhakal and Maekawa (2002). Original reinforcing bar properties suggested by Haber et. al (2013) are used as the properties of the reinforcing bar outside of the plastic hinge region as shown in Figure 4.2. Furthermore, material properties inside the plastic hinge region change because of intentional debonding and bar bond-slip as discussed subsequently.

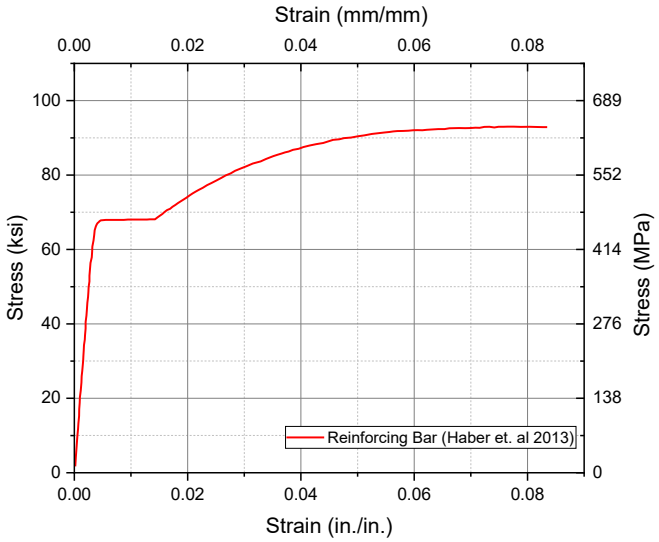


**Figure 4.2** Original Reinforcing bar properties (Haber et al. 2013)

### 4.3.3 Low Cycle Fatigue

When continuous cyclic load is applied in a repetitive manner, reinforcing bars start bending and straightening in a cycle, causing fatigue. Fatigue cycles formed due to repetitive loading cause fracture of reinforcing bars especially under high strains. The *ReinforcingSteel* material model includes low cycle fatigue by using the Coffin-Mason's expression (Manson 1965). Kunnath et al. (2009) presented a cumulative damage rule, which can be used with the Coffin-Manson model to predict fatigue during cyclic degradation.

$$\varepsilon^p = C_f\left(2N_f\right)^{-\alpha} \tag{1a}$$

$$D_f = \frac{1}{\sum_{i=1}^{n}(2N_f)_i} \tag{1b}$$

where, $\varepsilon^p$ is the plastic strain, $C_f$ and $\alpha$ are material constants equal to 0.26 and 0.506 respectively, and $2N_f$ is the number of half cycles to failure. The values of these parameters are altered to align them with experimental results (Mazzoni et al. 2006).

### 4.3.4 Bar Bond-slip and Debonding Model

To evaluate the bond-slip effect, three criteria must be considered: slip between the grout and reinforcing bar, slip effects due to intentional debonding of reinforcing bars, and the combined effect of bar-slip and intentional debonding. Since reinforcing bars experience bond slip, the strain will change in the debonded region. The modified stiffness of reinforcing bars due to this effect was calculated based on experimental results (Tazarv and Saiidi 2015). Tazarv and Saiidi (2015) constructed a constitutive bond-slip model for reinforcing bars with sufficient anchorage length, which included an initial elastic region and modified properties of the reinforcing bars in that region. These elastic properties were used where slippage in the bar would occur; slippage occurs between the grout and reinforcing bar known as rebar slip and at the region of bar debonding.

**Slip between grout and steel reinforcing bar**

The bond between the reinforcing bar and the grout begins to decline with continuous application of cyclic load. Bar bond-slip 1D springs can be used to calculate a modified stress vs. strain relationship of the reinforcing bar as (Tazarv and Saiidi 2015):

$$\varepsilon'_s = \varepsilon_s + \left(\frac{F}{k_b}\right)/L_{emb} \tag{2}$$

$$k_b = 78.5\, d_d\, L_{emb}\, u \tag{3}$$

$$u = \frac{9.5\sqrt{f'_{grout}}}{d_b} \tag{4}$$

where, $\varepsilon_s$ is bar strain, $F$ is the force in the reinforcing bar ($lbs$), $k_b$ is the bond-slip stiffness of bar ($lbs/in.$), $L_{emb}$ is the length of embedment ($in.$), $f'c$ is the compressive strength of concrete ($psi$), $f'_{\text{grout}}$ is the compressive strength of the grout ($psi$), $d_b$ $and$ $d_d$ are the diameter of bar and duct respectively ($in.$), and $f_s$ is the stress in the reinforcing bar ($psi$).

**Bar debonding model**

The chemical and frictional bond between reinforcing bar and grout or concrete is removed by wrapping duct tape around a reinforcing bar or using PVC pipes of tighter dimension around the reinforcing bar, known as intentional debonding technique. The normal stress-strain relationship used for reinforcing bars cannot be used in this case, since the intentionally debonded section tries to soften the connection prolonging failure time of reinforcing bar. Since the stress-strain behavior in the region where intentional debonding is carried out changes based on the amount of intentional debonding, modified material properties in that region must be used. Tazarv and Saiidi (2015) developed a numerical model, which could predict stress and strain change based on the amount of intentional debonding performed, which can be further modified based on the amount of intentional debonding carried out inside the footing.

$$\varepsilon'_s = \varepsilon_s + \left(\frac{F}{k_b}\right)/L_{emb} + \varepsilon_{elong} \tag{5}$$

$$\varepsilon_{elong} = \begin{cases} \gamma\frac{\varepsilon_s}{2} & f_s \le f_y \\ \gamma\left(\frac{\varepsilon_y}{2} + \frac{\varepsilon_s\, L^*}{2L_{emb}}\right) & f_s > f_y \end{cases} \tag{6}$$

$$L^* = \frac{(f_s - f_y)d_b}{4u_b} \le L_{emb} \tag{7}$$

$$u_b = 230\sqrt{f'_{grout}} \quad (8)$$

where $u_b$ is the bond stress developed in the grout (*psi*), and $\varepsilon_{elong}$ is the strain developed due to bar debonding.

Since $8d_b$ debonding for the Test 1 column was carried out inside the footing, full elongation was used, whereas, for the Test 2 column, only $4d_b$ intentional debonding was inside the footing. The elongation coefficient $\gamma$ used for Test 1 was assumed as 1.0 since the total amount of intentional debonding was achieved inside the footing; a total elongation coefficient $\gamma$ was set equal to 0.5 in Eq. (6) for the Test 2 column since only $4d_b$ intentional debonding was achieved inside the footing. The values obtained were used to develop a modified stress-strain curve of the reinforcing bar in the plastic hinge region.

Modified material properties were obtained inside the plastic hinge region based on Equations (2-8), which were used to calculate modified strain due to bond-slip and intentional debonding. Modified stress strain curves were developed where the slope of the linear section was computed to obtain the modified pseudo modulus of elasticity of the reinforcing bars in the plastic hinge region. The solid line shown in Figures 4.3 and 4.4 show the modified stress strain curve for Test 1 and Test 2 specimen, respectively. The dotted line in Figures 4.3 and 4.4 show the original reinforcing bar material as proposed by Haber et. al (2013). Different properties based on geometry and strength of materials, which were used to calculate modified stress-strain curve are shown in Table 4.1. Numerical values obtained from Table 2 were used in Equations (2-8) to find the modified strain value for each stress value. The embedded length for Test 1 was calculated as the sum of the length of intentional debonding and the length of the factory dowel inside the footing equal to 7.5 in. For Test 2 the embedded length was calculated as the sum of the length of intentional debonding, the length of the factory dowel inside the footing 7.5 in., and the reinforcing bar length, which is bonded to the footing concrete equal to 4.0 in.

**Table 4.1** Properties used to calculate the modified strain in the column reinforcing bars

| Parameter *(units)* | Test 1 | Test 2 |
|---|---|---|
| $l_{emd}$ *(in.)* | 15.5 | 19.5 |
| $d_d$ *(in.)* | 3.12 | 3.12 |
| $d_b$ *(in.)* | 1.0 | 1.0 |
| $f'c$ *(ksi)* | 10.7 | 10.7 |
| $f'_{grout}$ *(ksi)* | 15.1 | 16.3 |
| $k_b$ *(lbs/in.)* | 4431680 | 5792640 |
| $u_b$ *(psi)* | 3690 | 3830 |

The modified material properties were used in the numerical model at a column section where bond-slip was expected and intentional debonding was present, i.e., the plastic hinge region. The slope of the modified steel stress-strain curve for reinforcing bars was calculated up to the elastic limit. The modified modulus of elasticity was found as $Es_1$= 14185 ksi and $Es_2$ = 19130 ksi for Test 1 and Test 2 experiments, respectively. The modified modulus of elasticity determined from the modified stress strain curve was used to account for both bar slip and debonding effects in the plastic hinge region (Tazarv and Saiidi 2015; Ameli and Pantelides 2017). The modified properties of the steel reinforcing bar acquired can be esd to determine the section's actual behavior in the plastic hinge region.

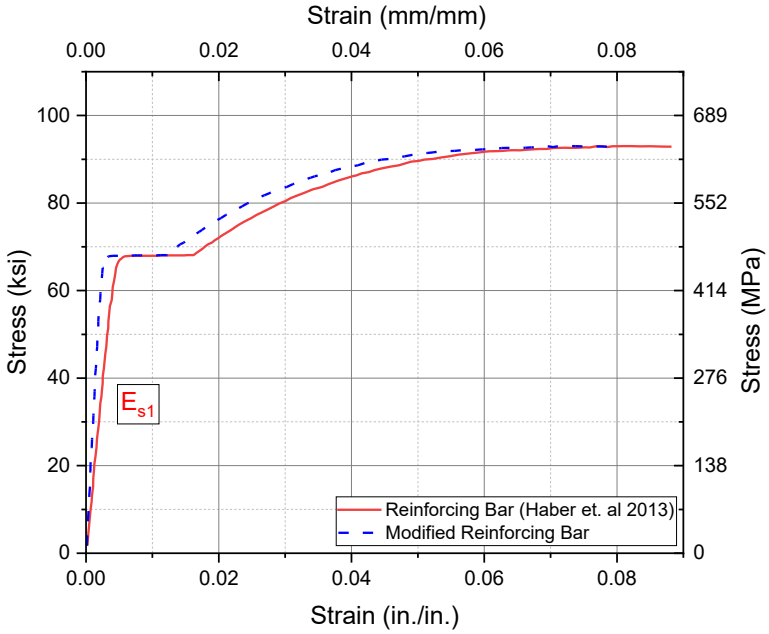


**Figure 4.3** Stress-strain curve for original and modified reinforcing bar (Test 1)

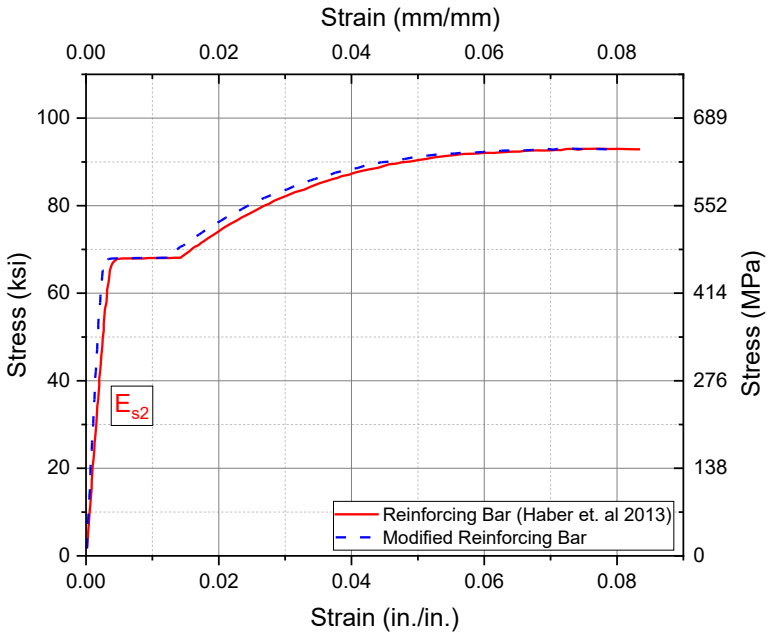


**Figure 4.4** Stress-strain curve for original and modified reinforcing bar (Test 2)

### 4.3.5 Bar Buckling Model

The buckling model proposed by Dhakal and Maekawa (2002) is used to model reinforcing bar buckling. The model requires two parameters to incorporate buckling of reinforcing bars: slenderness ratio and amplification factor. The value of the amplification factor depends on whether the material shows linear strain hardening behavior or elastic perfectly plastic material behavior. In the general case, the material is assumed as linear strain hardening material and the value of amplification factor is assumed to be 1.0.

## 4.4 Beam-Column Elements

The reinforced concrete column is modeled using fiber-based elements. Each section of fiber represents a different stress-strain behavior. The *forceBeamColumn* element, which is based on an iterative force-based formulation, was used to represent the column. The octagonal column shape was represented with an equivalent circular section, and the *Section* command was used to create the composite section. The circular section is divided into 20 radial divisions and 40 circumferential divisions for the core concrete, and five radial divisions and 40 circumferential divisions for the cover concrete, respectively. The *Patch* command was used to construct the core and cover concrete subdivisions. Six longitudinal bars were modeled using the *Layer* command in OpenSees. The *forceBeamColumn element* can also use plastic hinge length as a one of the parameters. Instead of using integration points, plastic hinge length was used to numerically model the actual behavior of the column. The schematic of the beam column element formulation model is shown in Figure 4.5.

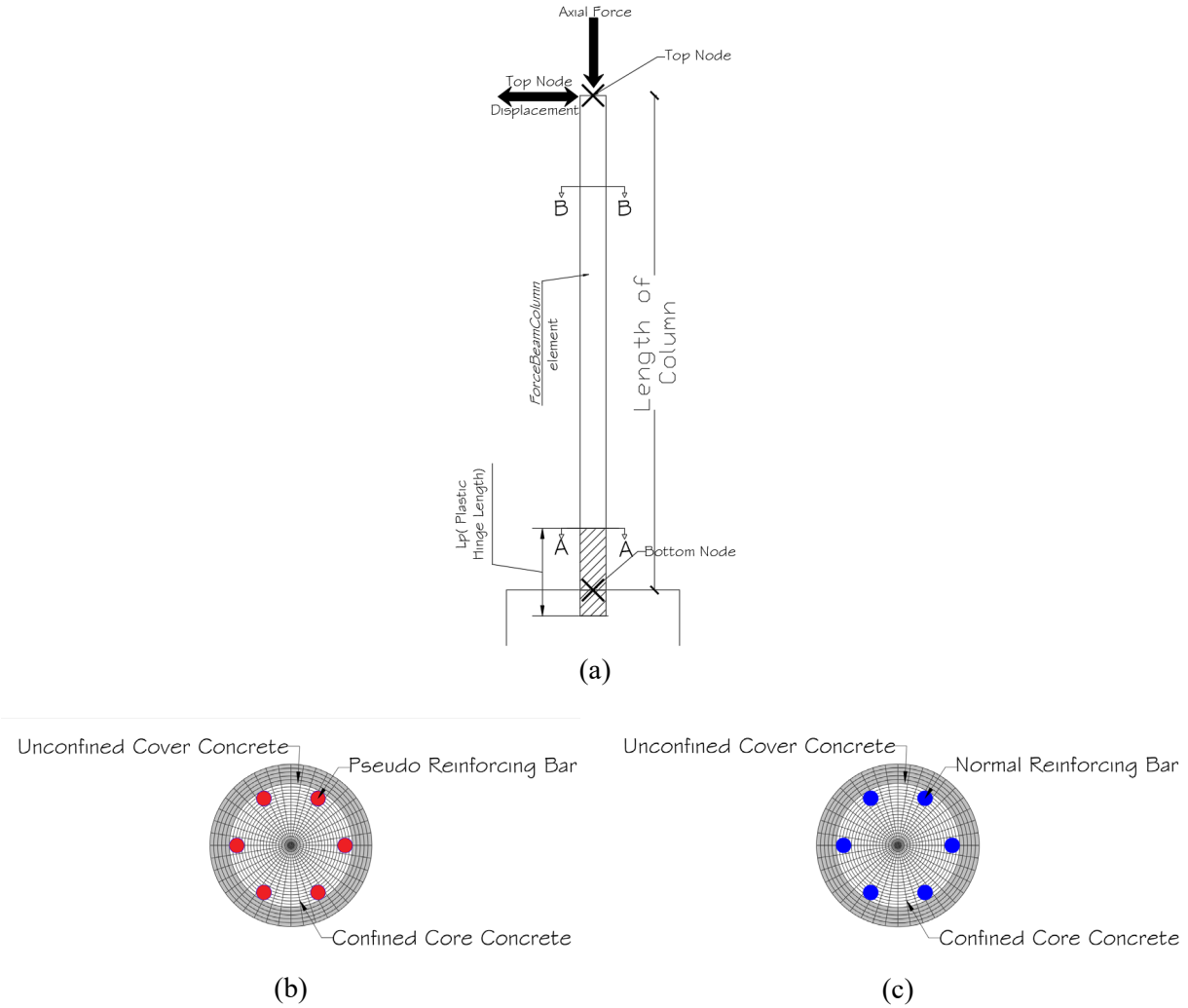


**Figure 4.5** Model schematic: (a) model layout; (b) cross-section inside plastic hinge; and (c) cross-section outside plastic hinge

## 4.5 Plastic Hinge Length $(L_p)$

The AASHTO Guideline Specification (2011) and Caltrans Seismic Design Criteria (2010) are widely used for the design of bridges in the United States (AASHTO 2011, 2020) with other Department of Transportation (DOT) guidelines. To simulate the experimental performance, the numerical model must be able to estimate the plastic hinge length. An approach by Panagiotakos and Fardis (2001) appears to correspond well with the experimental values and was used to determine plastic hinge length as follows:

$$L_p = 0.12H + 0.095a_{sl}d_b f_y \quad (9)$$

where, $a_{sl}$ is equal to zero when bar pullout is restricted and is equal to 1.0 if the reinforcing bar is allowed to pull out; $d_b$ is the longitudinal bar diameter (in.); $H$ is the height of the column specimen (in.); and $f_y$ is the yield strength of the reinforcing bar (ksi).

The plastic hinge length for the proposed model is based on the stress-strain curve from experiments conducted by Barton et al. (2022); the experiments conducted had intentional debonding and a galvanized duct connected to a grouted spliced sleeve and estimation of the actual plastic hinge length is not trivial. The assumed strain distribution in the reinforcing bars, based on the two experiments, is shown in Figure 4.6; the value of multiplier $\alpha$ varies from 1.0 to 2.0, whereas the value of multiplier $\beta$ is between 18.0 to 20.0 from the tests, where $\varepsilon_y$ is the yield strain of the reinforcing bar. The plastic hinge length was evaluated by comparing the numerical model response with the experimental results. The plastic hinge length is defined here as the sum of the plastic hinge length of the cast in place (CIP) specimen as proposed by Ameli and Pantelides (2017) and the length of debonding inside the footing. The plastic hinge length for the CIP specimen was 12 in. and the amount of debonding for Test 1 was 8 in. inside the column-to-footing interface, resulting in a total plastic hinge length of 20 in. For Test 2 the amount of debonding inside the footing surface was 4 in., resulting in a total plastic hinge length of 16 in., as shown in Figure 4.7(a, b, c).

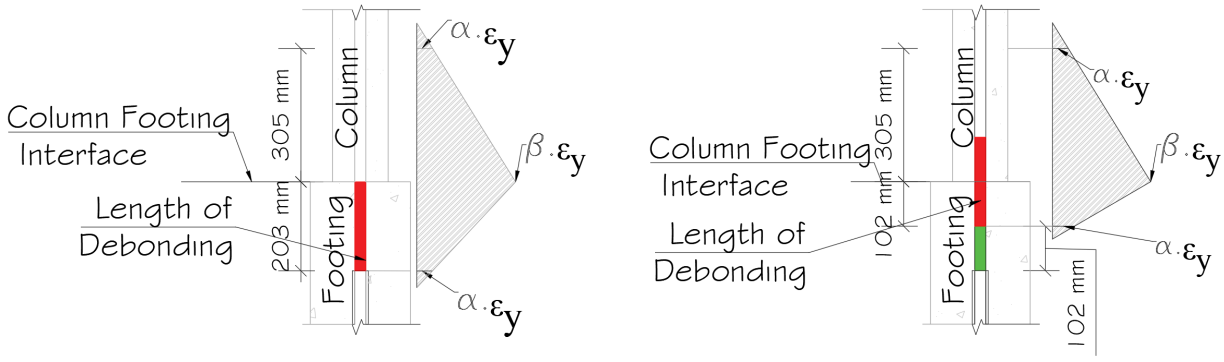


**Figure 4.6** Strain distribution plot (Barton et al. 2022)

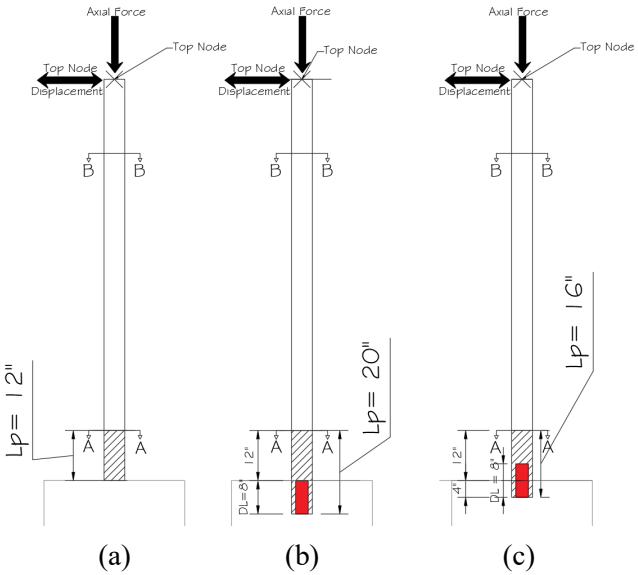


**Figure 4.7** Plastic hinge length representation (a) CIP; (b) Test 1; and (c) Test 2
Note: DL = debonding length; Lp = length of plastic hinge

## 4.6 Analysis

Static analysis in OpenSees was used for gravity and cyclic loads. By applying a unidirectional pull up to a certain drift ratio, pulling back to that same drift ratio in the other direction, and then pushing back to a zero-drift ratio, a cyclic analysis was carried out. The *DisplacementControl* integrator object performed the static analysis, which implies that the analysis was displacement-controlled, so each subsequent analysis step was performed at each incremental displacement at one degree of freedom. For all static studies, the displacement increment was set at 1.0% of the column height. To use a reliable approach for resolving non-linear algebraic equations, *Newton*, *Broyden NewtonLineSearch*, and *KrylovNewton* were used to solve the non-linear residual problem at each time step (Bowman 2016).

## 4.7 Comparison of Experiments and Numerical Model

To assess the behavior of the bridge bent specimen under a quasi-static lateral cyclic load coupled with an axial load, an analytical model was created in OpenSees. As mentioned in the preceding sections, an analytical model was created, and numerical results were verified with the experimental results. The initial stiffness, lateral strength, and hysteretic energy dissipation capacity of the test were successfully captured by the numerical model, which also closely matched the outcomes of the experiment. The lateral load vs. drift ratio (hysteretic curve) is shown in Figure 4.8 with experimental and numerical model findings. The hysterical behavior of the experiment may be predicted by the model.

The numerical model dissipated a comparable amount of total hysteretic energy as in the actual experiment, as shown in Figure 4.9. The error in cumulative hysteretic energy was found to be 6% and 2% between numerical model and experiment for Test 1 and Test 2, respectively. The error in cumulative hysteretic energy suggests good alignment of the numerical model with the actual experiment. In addition, the numerical model could predict the local response in terms of bar fracture. The precise cycle in which the reinforcing bar fractured during the experiment was also captured by the numerical model, confirming good agreement.

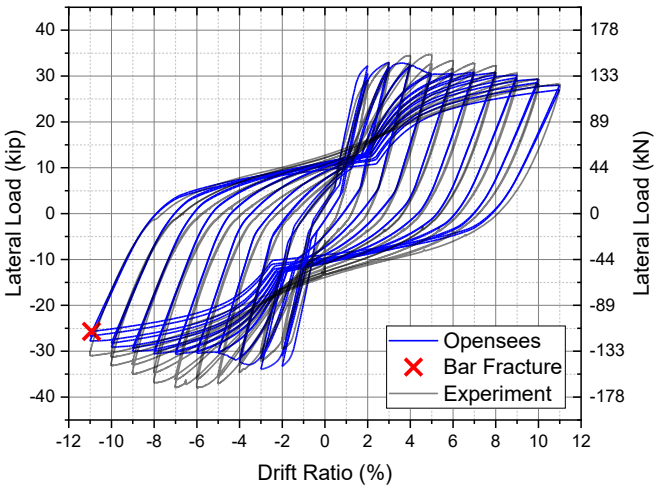


(a)

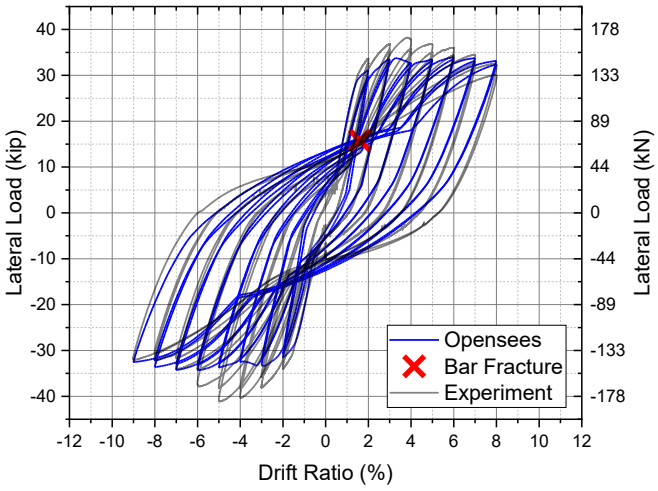


(b)

**Figure 4.8** Hysteretic performance: (a) Test 1; and (b) Test 2

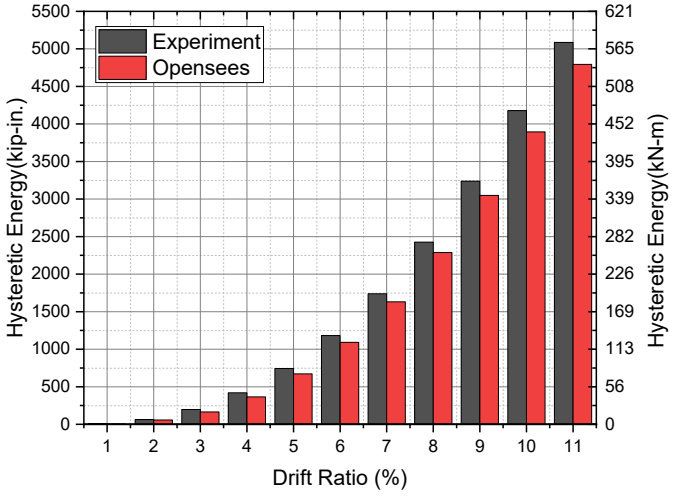


(a)

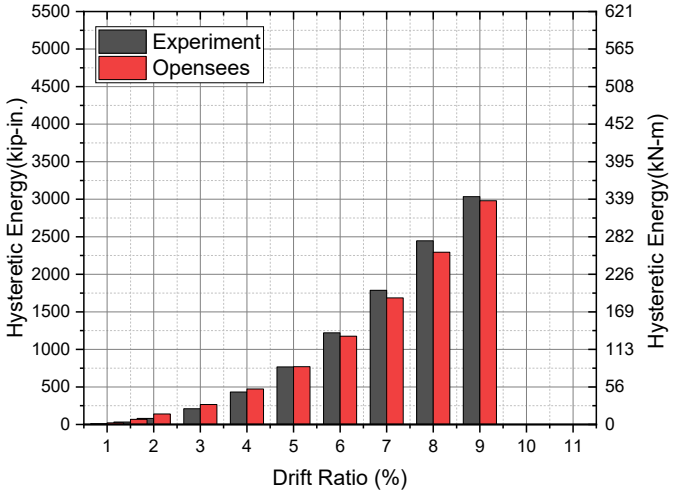


(b)

**Figure 4.9** Cumulative hysteretic energy comparison between numerical model and experiment: (a) Test 1; and (b) Test 2

# 5. PARAMETRIC STUDY

The numerical study performed for the two half-scaled specimens predicted the experimental response with sufficient accuracy. To extend the usefulness of the numerical model, a parametric study was carried out for an as-built three-column bridge bent of an actual bridge. The parametric study was performed for a monolithic specimen at first and was compared with the experiment performed by Pantelides et al. (2004). The actual bridge bent with existing seismic details was studied at first and the seismic details were modified according to new bridge seismic specifications. The actual three-bridge bent was the bridge bent at South Temple Bridge (bent #5S) in Salt Lake City, Utah.

## 5.1 As Built Three-column Bridge Bent

The actual bridge bent consisted of three columns, a cap beam and the soil-resisting pile foundation system. The bridge columns had a square cross section 36 in. x 36 in. The columns were reinforced with 16 #10 longitudinal reinforcing steel bars; #4 ties were used at 12 in. spacing on center. Since the spacing of the ties was large with insufficient seismic details, the column was not confined adequately, resulting in substandard seismic performance. Figure 5.1 shows the as-built bridge bent with the column cross-section details tested by Pantelides et al. (2004). The numerical model for the as-built bridge bent was developed based on the material properties obtained during the test. The concrete compressive strength was found to be 4.9 ksi and the yield strength of the mild steel reinforcing bar was measured to be 48.7 ksi. Material properties based on these strengths were used in a numerical model and compared with the test results.

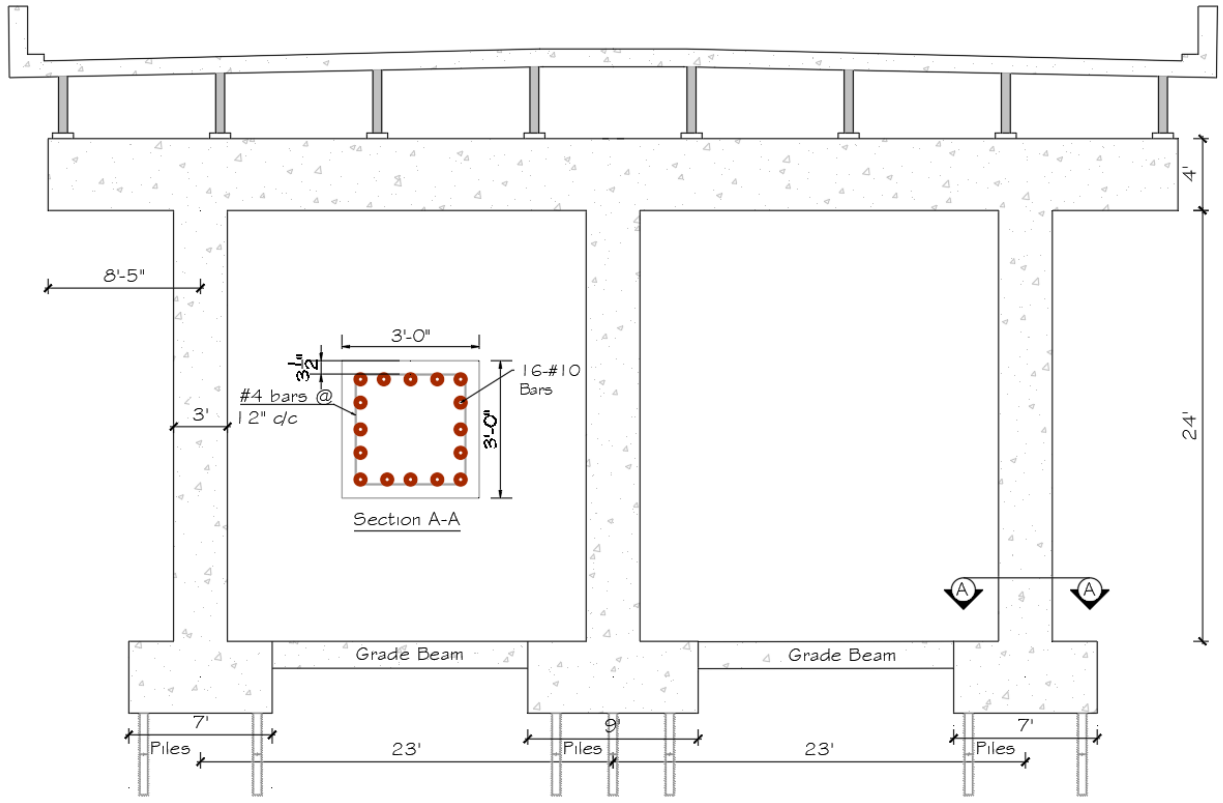


**Figure 5.1** As-built bridge bent #5s (Pantelides et al. 2004)

### 5.1.1 Numerical Model

The numerical model used in the verification of Test 1 and Test 2 specimens discussed in sections 4.3-4.5 was modified to represent the actual bridge bent. A 2D numerical model consisting of the cap-beam, bridge columns, and foundation including the soil structural springs was created. To prepare such a numerical model, the joints between the columns and cap-beam were defined as rigid joints. Mander's model was used to model the concrete properties and *Concrete04* element present in OpenSees was used to model the concrete. The steel reinforcing bars were modeled as *ReinforcingSteel* material, and different material properties inside and outside the plastic hinge regions were used. The modified pseudo reinforcing property due to bond-slip in the case of the actual three-column bridge bent was computed using the equations discussed in section 4.3. The modified modulus of elasticity of the columns for the actual bridge bent was found to be 24,160 ksi, and this property was used for modeling the reinforcing bars inside the plastic hinge regions. The column cross section was divided into 15 subdivisions — both width- and height-wise — for the cover and core concrete. The column cap-beam and the grade beam connecting the columns to the base of the footing were modeled as *elasticBeamColumn* elements. The interaction between column and cap beam was made rigid using rigid links to connect both parts. The weight of the deck was considered and modeled as nodal mass at each node of the cap-beam. The nodal mass for node 8, 9 and 10 was found as 0.9478 k-s$^2$/in., 0.9669 k-s$^2$/in. and 0.9478 k-s$^2$/in. respectively. Nodes 8,9 and 10 can be seen in the schematic layout of Figure 5.2. The axial load plays an essential role in predicting the behavior of the numerical model and in defining whether the proposed numerical model is in good agreement with the experiment. A 6% of Axial Load Index (ALI) i.e., 305.4 kip was applied as axial load for each column.

It is essential to predict the actual plastic hinge length ($L_p$) of the columns of the structure. To evaluate the plastic hinge length of the columns for the actual as-built bridge bent, the equation proposed by Panagiotakos and Fardis (2001) was used. Equation (9) with the reinforcing bars restricted against pullout was used to calculate the plastic hinge length of the columns; the plastic hinge length was found to be 12% of the length of column or 17.28 in. Two different numerical models were prepared — one without soil structure interaction (SSI) i.e., fixed-base numerical model; the other included SSI. The fixed-base numerical model was prepared without considering the pile foundation and the bottom node of each column was assumed to be a fixed support; the model with SSI contained a total of 60 equivalent frictional soil springs to represent the soil-pile cap and soil-grade beam behavior (Wu and Pantelides 2019). The numerical model was used to predict the response of the three-column bridge bent and was compared to the experimental results.

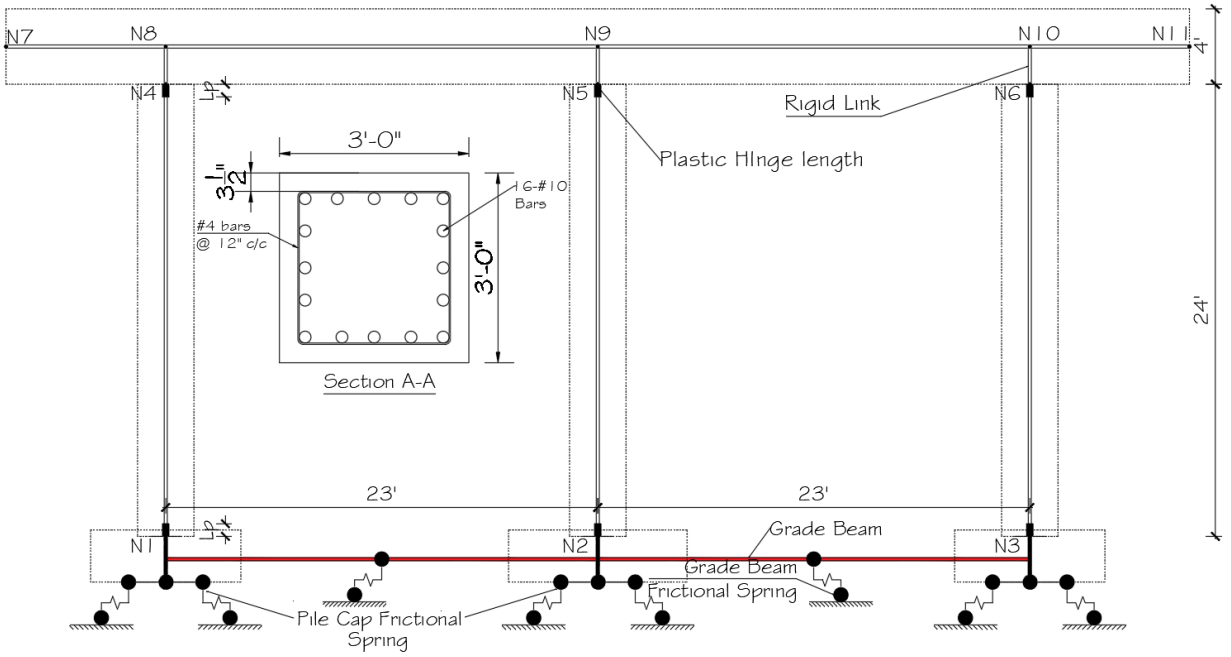


**Figure 5.2** Schematic for numerical model of 3-column bridge bent (as built bridge bent)

### 5.1.2 Results and Comparison with Experiment

The numerical model, including the weight of the deck, was loaded with cyclic displacement-controlled loading. The response was recorded for both the fixed base type numerical model and the numerical model with SSI. The cyclic envelope thus obtained was plotted with the cyclic envelope obtained from the cyclic-displacement controlled test performed by Pantelides et al. (2004). The structural response showed that the numerical model predicted the response well by matching the experimental results, as shown in Figure 5.3. The results showed that, when the numerical model is prepared with a fixed base, it has a slightly higher initial stiffness than that of the numerical model with SSI.

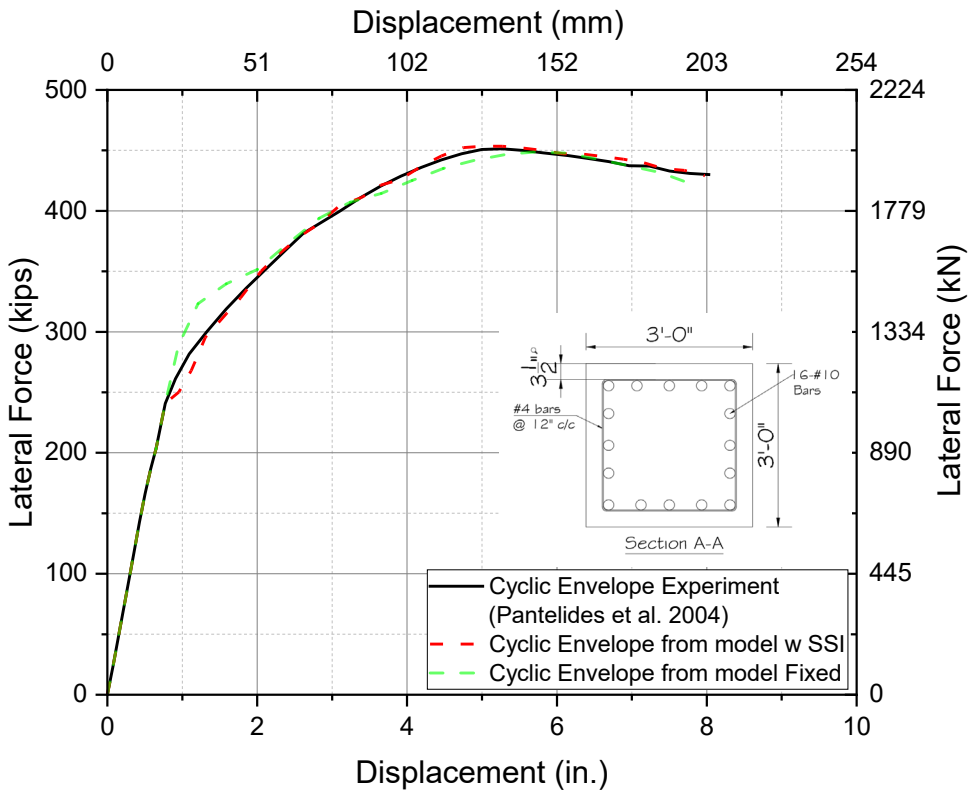


**Figure 5.3** Envelope of cyclic load vs. displacement for three-column bridge bent tested by Pantelides et al. (2004) considering fixed base and SSI

## 5.2 Three-column Bridge Bent with New Seismic Details

This is a slight modification of the as-built bridge bent using the same geometry and loading as that of the as-built bridge bent but with changes in the number and spacing of the confining seismic hoops in the columns. This bridge bent consisted of three columns, a cap beam and the foundation with the soil resisting pile system. The bridge columns had the same dimensions and longitudinal reinforcement; however, #4 ties were used at 2.5 in. spacing on center with improved seismic details. Figure 5.4 shows the as-built beam and the cross section of the column with new seismic details.

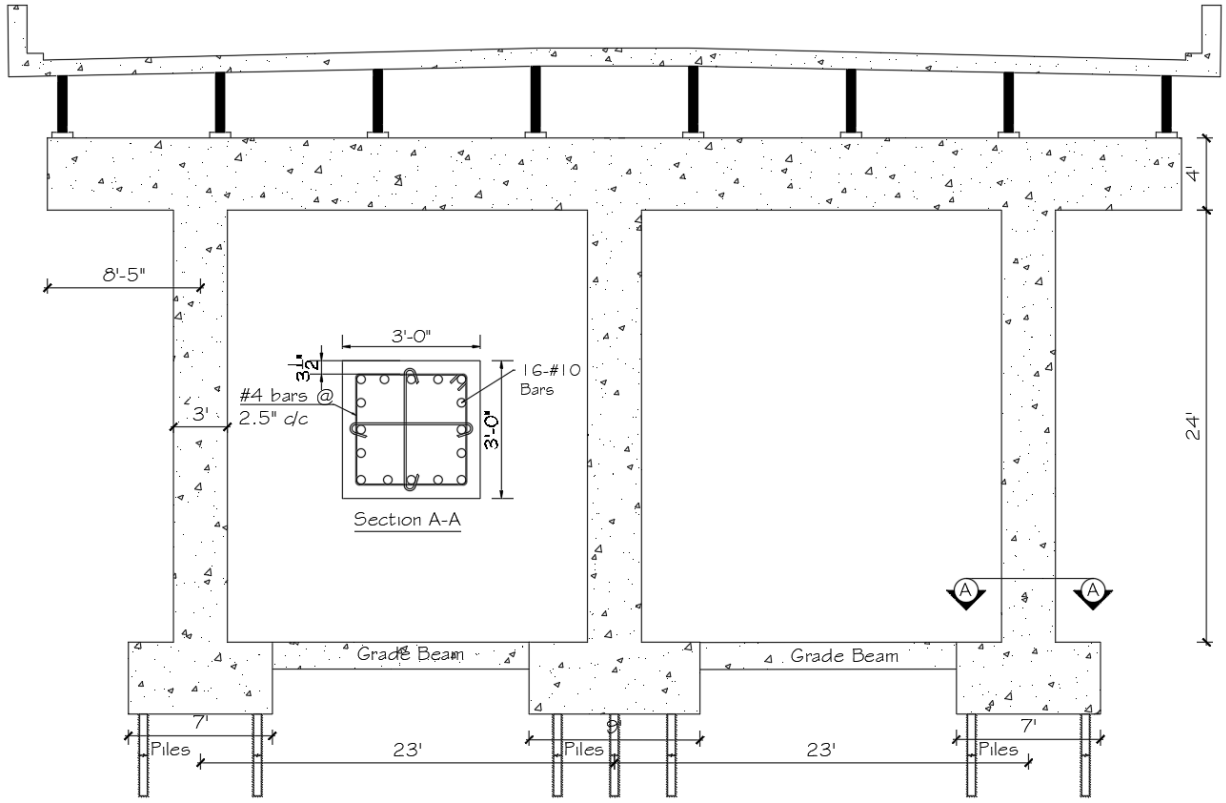


**Figure 5.4** Three-column bridge bent with new seismic details

### 5.2.1 Numerical Model

A 2D numerical model, consisting of a cap-beam, bridge columns, foundation and the soil structural springs, was prepared. After the actual as-built bridge bent performance was verified with the numerical results, as shown in Figure 5.5, three types of future bridge bents were prepared. One bridge bent with new seismic details and monolithic in construction, termed the cast in place bent (CIPB); the remaining two bridge bents utilized details similar to the precast Type 1 and Type 2 precast specimens. The first precast specimen was prepared in such a way that it had $8d_b$ intentional debonding inside the footing as in Test 1 case and was named as precast bent 1 (PCB1). The second precast bridge bent had intentional debonding distributed equally in the column and footing and was named precast bent 2 (PCB2). The connection details of the reinforcing bars extending from the column to the footing and the cap-beam are shown in Figure 5.5.

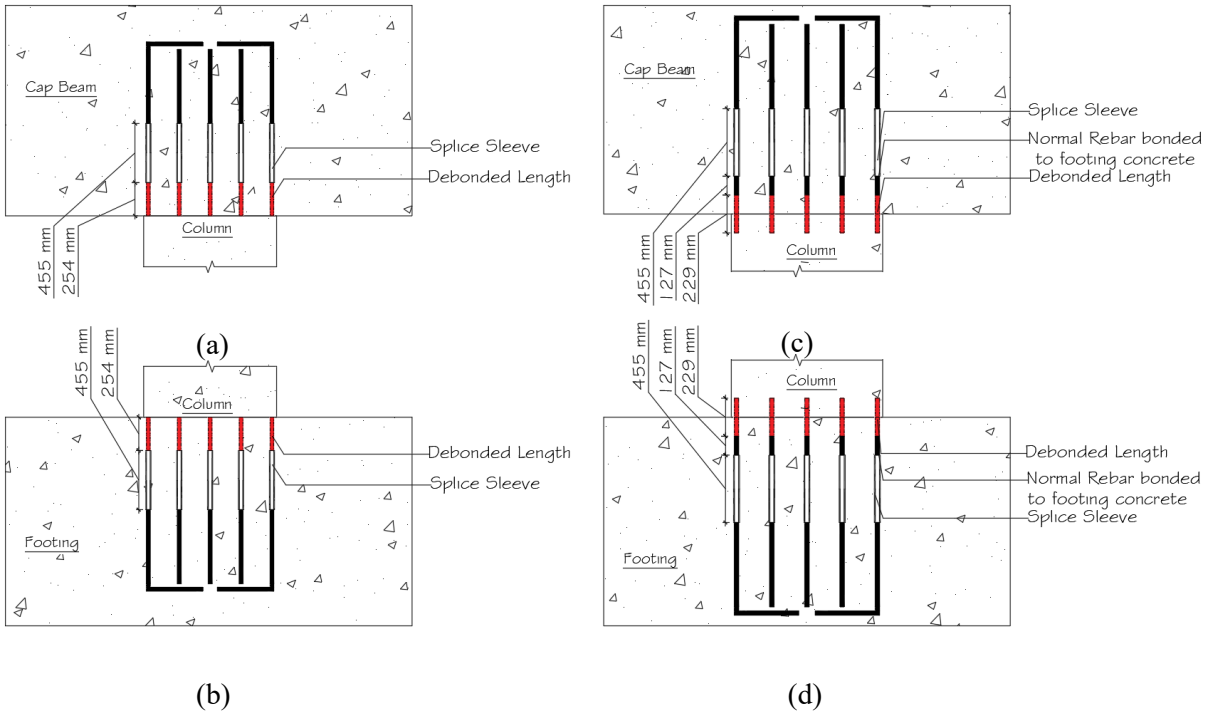


**Figure 5.5** Connection details at interface for precast bridge bents: (a) PCB1 at cap-beam; (b) PCB1 at footing; (c) PCB2 at cap-beam; and (d) PCB2 at footing

Material properties of concrete with higher amount of confinement were used from Mander's model. Steel reinforcing bars were modeled as *ReinforcingSteel* material, and different material properties inside and outside the plastic hinge region were used. The modified pseudo modulus of elasticity and length of the plastic hinge used for CIPB, PCB1 and PCB2 are listed in Table 5.1.

**Table 5.1** Properties used in modeling (Bent with new seismic details)

| Type of bridge bent | Length of plastic hinge ($L_p$) (in.) | Pseudo modulus of elasticity($E_{smod}$) (ksi) |
|---|---|---|
| CIPB | 17.28 | 24,160 |
| PCB1 | 26.28 | 17,610 |
| PCB2 | 21.78 | 21,320 |

Similar to the as-built bridge bent column cross section the column section was divided into 15 subdivisions — both width- and height-wise — for the cover and core concrete. The column cap-beam and the grade beam connecting base of the footing were modeled as *elasticBeamColumn* elements. The interaction between column and cap beam was made rigid using rigid links to connect both specimens. The deck's weight was taken into account and transferred as nodal mass in each cap-beam node as previously described to nodes 8, 9, and 10 indicated in the schematic layout in Figure 5.6. For each case, the numerical model was prepared with SSI and a cyclic analysis was performed. The cyclic envelope and pushover curves obtained from the numerical model were plotted together and the cyclic envelope, which incorporated low-cycle fatigue was used as the capacity curve for each type of bridge bent: CIPB, PCB1 and PCB2.

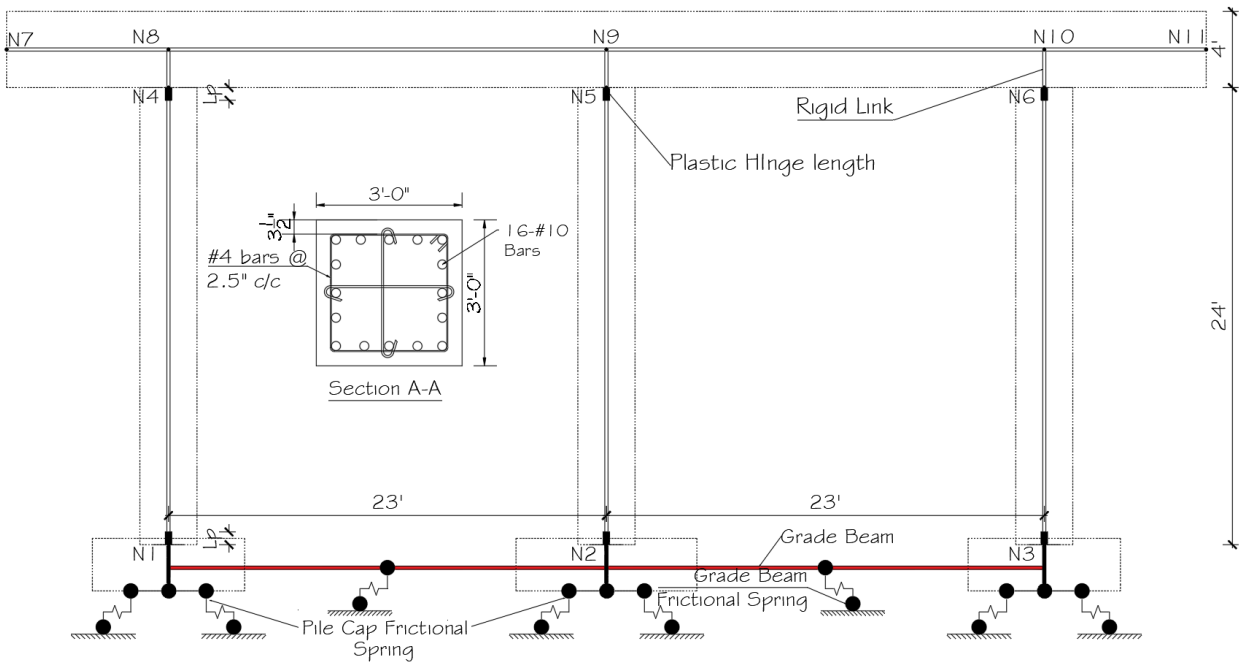


**Figure 5.6 Schematic diagram of the numerical model (new seismic details)**

### 5.2.2 Results

Cyclic and pushover analysis for the CIPB, PCB1 and PCB2 bents was carried out; the envelope of cyclic analysis results was prepared and plotted together with the static pushover and analytical hysteretic loops. The cyclic envelope showed failures occurring prior to the monotonic pushover curve. This is the case, since cyclic loading includes low-cycle fatigue and hence the cyclic envelope was used as a capacity curve for time-history analysis of the structure with different arrangements. Figure 5.7 (a, b, c) shows cyclic hysteretic curves, the cyclic envelope, and the pushover curve with failure points for bridge bents CIPB, PCB1 and PCB2, respectively.

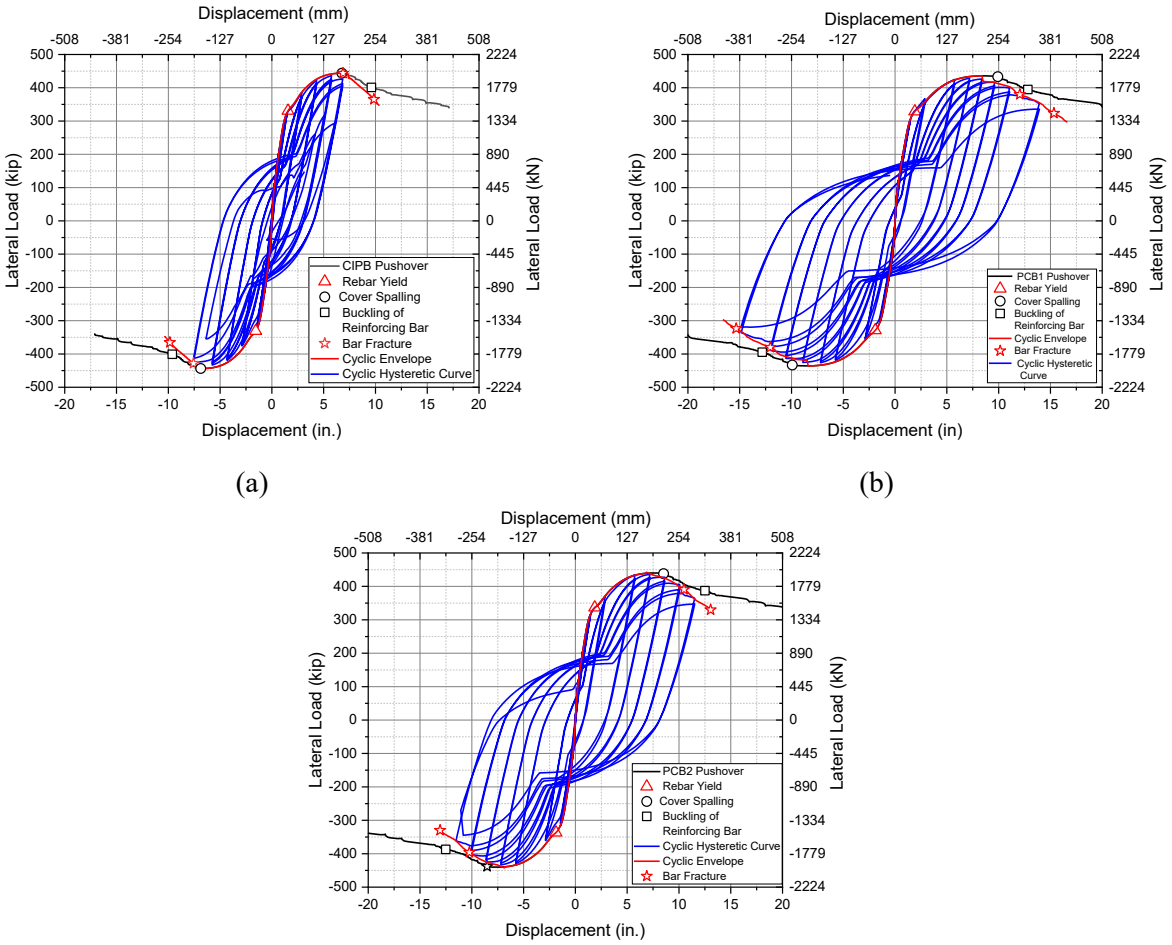


**Figure 5.7** Cyclic load vs. displacement curves and envelope for three-column bridge bent with new seismic details: (a) CIPB; (b) PCB1; and (c) PCB2

## 5.3 Non-linear Time-history Analysis

For significant bridges in seismic areas, nonlinear dynamic analysis is recommended. The time history may be used to examine displacement ductility, assess displacement demand, and evaluate the capacity of a real bridge. According to AASHTO Guide Specifications, spectrally matched ground motion data are employed for time-history analysis (AASHTO 2011, 2020). For various bridge sites, ground motion recordings with seismic characteristics may be obtained using the PEER Ground Motion Database. Based on the earthquake magnitude, the faulting process, how near the rupture occurred, and the site conditions, ground motion data are chosen. Near-field and far-field earthquakes with pulsed and non-pulsed ground movements are studied to completely understand the dynamic behavior.

Base-corrected acceleration records are used to carry out non-linear time history analysis. The acceleration records are transformed to find the primary component of ground motion (Bartlett 2004). Response spectra is matched with the target spectrum and based on those matched response spectra, time-history data is computed and used for analysis of the full-scaled bridge bents.

The design spectrum was obtained from the USGS map for Salt Lake City and the exact coordinates of the bridge site; the site class was assumed as D. The response spectra given by earthquakes, which had a probability of exceedance of 10% in 50 years was used as the Design Based Earthquake (DBE); the 2% probability of exceedance in 50 years was used as the Maximum Credible Earthquake (MCE). The USGS design short period was 1.012 s and 1.518 s for the DBE and MCE, respectively. The fundamental period of the bridge bent was found to be 0.43 s, which came under the plateau of the response spectrum. The seismic performance of the three-bridge bent was studied using 22 Far-Field (FF) and 14 pulse type Near-Field (NF) earthquakes (Upadhyay et al. 2019). These ground motions were matched to the DBE and MCE level earthquake based on the fundamental period. Scaled Ground Motion (GM) data was used as the time-history input for the dynamic analysis of the three-column bridge bents. Table 5.2 and Table 5.3 show the details of the NF and FF earthquakes that were used. Figure 5.8 shows the unmatched response spectra at the DBE level for both FF and NF earthquakes and Figure 5.9 shows the matched response spectra for the DBE and MCE level.

**Table 5.2** Far-Field Earthquakes

| GM Number | Earthquake | | | Recording Station | Epicentral Distance (km) | PGA (g) |
|---|---|---|---|---|---|---|
| | M | Name | Year | | | |
| FF1 | 6.7 | Northridge | 1994 | Beverly Hills - Mulhol | 13.3 | 0.52 |
| FF2 | 6.7 | Northridge | 1994 | Canyon Country-WLC | 26.5 | 0.48 |
| FF3 | 7.1 | Duzce, Turkey | 1999 | Bolu | 41.3 | 0.82 |
| FF4 | 7.1 | Hector Mine | 1999 | Hector | 26.5 | 0.34 |
| FF5 | 6.5 | Imperial Valley | 1979 | Delta | 33.7 | 0.35 |
| FF6 | 6.5 | Imperial Valley | 1979 | El Centro Array #11 | 29.4 | 0.38 |
| FF7 | 6.9 | Kobe, Japan | 1995 | Nishi-Akashi | 8.7 | 0.51 |
| FF8 | 6.9 | Kobe, Japan | 1995 | Shin-Osaka | 46 | 0.24 |
| FF9 | 7.5 | Kocaeli, Turkey | 1999 | Duzce | 98.2 | 0.36 |
| FF10 | 7.5 | Kocaeli, Turkey | 1999 | Arcelik | 53.7 | 0.22 |
| FF11 | 7.3 | Landers | 1992 | Yermo Fire Station | 86 | 0.24 |
| FF12 | 7.3 | Landers | 1992 | Coolwater | 82.1 | 0.42 |
| FF13 | 6.9 | Loma Prieta | 1989 | Capitola | 9.8 | 0.53 |
| FF14 | 6.9 | Loma Prieta | 1989 | Gilroy Array #3 | 31.4 | 0.56 |
| FF15 | 7.4 | Manjil, Iran | 1990 | Abbar | 40.4 | 0.51 |
| FF16 | 6.5 | Superstition Hills | 1987 | El Centro Imp. Co. | 35.8 | 0.36 |
| FF17 | 6.5 | Superstition Hills | 1987 | Poe Road (temp) | 11.2 | 0.45 |
| FF18 | 7 | Cape Mendocino | 1992 | Rio Dell Overpass | 22.7 | 0.55 |
| FF19 | 7.6 | Chi-Chi, Taiwan | 1999 | CHY101 | 32 | 0.44 |
| FF20 | 7.6 | Chi-Chi, Taiwan | 1999 | TCU045 | 77.5 | 0.51 |
| FF21 | 6.6 | San Fernando | 1971 | LA - Hollywood Stor | 39.5 | 0.21 |
| FF22 | 6.5 | Friuli, Italy | 1976 | Tolmezzo | 20.2 | 0.35 |

**Table 5.3** Near-Field Earthquakes

| GM Number | Earthquake | | | Recording Station | Epicentral Distance (km) | PGA |
|---|---|---|---|---|---|---|
| | M | Name | Year | | | |
| NF1 | 6.5 | Imperial Valley-06 | 1979 | El Centro Array #6 | 27.47 | 0.4 |
| NF2 | 6.5 | Imperial Valley-06 | 1979 | El Centro Array #7 | 27.64 | 0.4 |
| NF3 | 6.9 | Irpinia, Italy-01 | 1980 | Sturno | 30.35 | 0.3 |
| NF4 | 6.5 | Superstition Hills-02 | 1987 | Parachute Test Site | 15.99 | 0.4 |
| NF5 | 6.9 | Loma Prieta | 1989 | Saratoga - Aloha Ave | 27.23 | 0.3 |
| NF6 | 6.7 | Erzican, Turkey | 1992 | Erzincan | 8.97 | 0.4 |
| NF7 | 7 | Cape Mendocino | 1992 | Petrolia | 4.51 | 0.6 |
| NF8 | 7.3 | Landers | 1992 | Lucerne | 44.02 | 0.7 |
| NF9 | 6.7 | Northridge-01 | 1994 | Rinaldi Receiving Sta | 10.91 | 0.8 |
| NF10 | 6.7 | Northridge-01 | 1994 | Sylmar - Olive View Med FF | 16.77 | 0.7 |
| NF11 | 7.5 | Kocaeli, Turkey | 1999 | Izmit | 5.31 | 0.2 |
| NF12 | 7.6 | Chi-Chi, Taiwan | 1999 | TCU065 | 26.67 | 0.8 |
| NF13 | 7.6 | Chi-Chi, Taiwan | 1999 | TCU102 | 45.56 | 0.2 |
| NF14 | 7.1 | Duzce, Turkey | 1999 | Duzce | 1.61 | 0.5 |

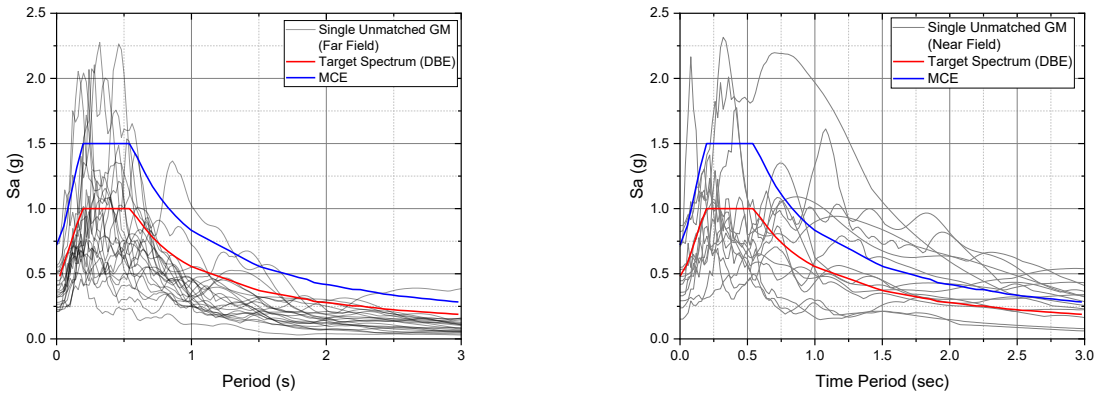


(a) (b)

**Figure 5.8** Scaled response spectrum for three-column bridge bent; a) Far-Field DBE and MCE b) Near-Field DBE and MCE

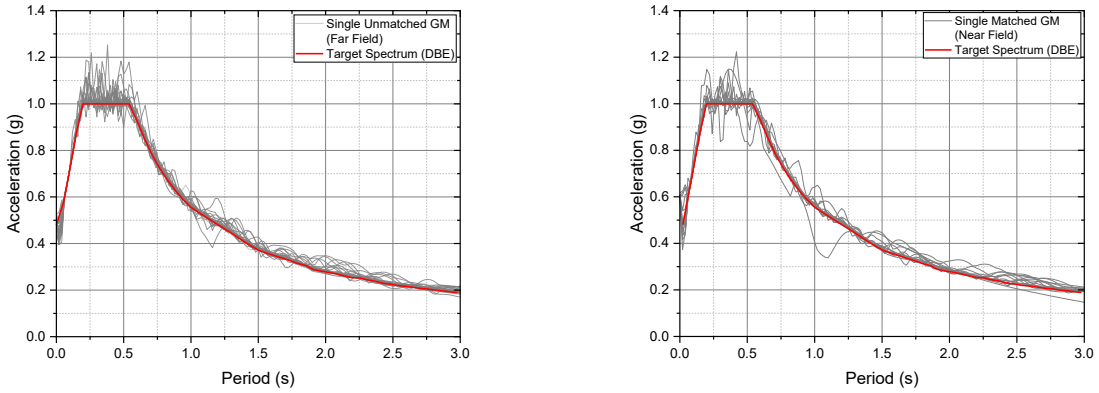


(a) (b)

**Figure 5.9** Matched response spectrum for three-column bridge bent; a) Far-Field DBE b) Near-Field DBE

### 5.3.1 Demand-to-capacity Representation

The capacity curve for each bent (CIPB, PCB1 and PCB2) was computed from cyclic analysis. The capacity curve was the envelope of cyclic load vs. displacement. Two major parameters involving the drift ratio were utilized: the drift ratio at which the specimen had failed, and the drift ratio at maximum lateral load; these points were marked for capacity curve. A similar calculation was carried out for each type of bridge bent when 22 FF and 14 NF earthquakes were assumed to occur. The results obtained by time-history analysis were considered the demand due to ground motions (GMs). These demands were calculated for each FF and NF earthquakes for both the DBE and MCE level. After obtaining the demand values, they were used to calculate the demand-to-capacity ratio at maximum ultimate drift ratio and the demand-to-capacity ratio for the drift ratio at maximum lateral load. Figure 5.10 shows the representation of demand-to-capacity ratio. Using Equations (10) and (11), the demand-to-capacity ratio for the maximum drift ratio and the demand-to-capacity ratio for the drift ratio at maximum lateral load can be computed.

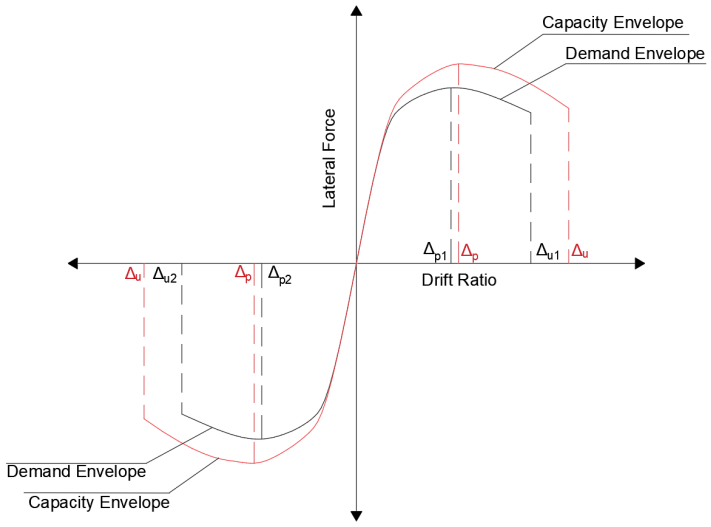


**Figure 5.10** Demand-to-capacity representation

where,
$\Delta_u$ is the maximum drift displacement capacity obtained from cyclic envelope (capacity envelope)
$\Delta_{u1}$ is the maximum positive drift displacement obtained from GM data (demand envelope)
$\Delta_{u2}$ is the maximum negative drift displacement obtained from GM data (demand envelope)
$\Delta_p$ is the drift displacement at maximum lateral load obtained from cyclic envelope (capacity envelope)
$\Delta_{p1}$ is the drift displacement at maximum positive lateral load obtained from GM data (demand envelope)
$\Delta_{p2}$ is the drift displacement at maximum negative lateral load obtained from GM data (demand envelope)

Demand-to-capacity ratio for maximum drift ratio:

$$DC_{maxdrift} = \frac{absolutemax(\Delta_{u1} and\ \Delta_{u2})}{\Delta_u} \quad (10)$$

Demand-to-capacity ratio for drift ratio at maximum lateral load:

$$DC_{drift@maxload} = \frac{absolutemax(\Delta_{p1} and\ \Delta_{p2})}{\Delta_p} \quad (11)$$

### 5.3.2 Results from Time-history Analysis

After scaling the GMs to the target spectrum, time history (TH) analysis was performed and the results for each ground motion were examined. The variation of the top node displacement was studied with time. Figure 5.11 shows the top node displacement for the FF19 (Chi-Chi, Taiwan) and NF12 (Chi-Chi, Taiwan) earthquakes. The top node TH analysis shows the propagation and variation of the displacement amplitude. The load vs. displacement curve shows the hysteretic performance of the bridge bents due to a specified earthquake. This hysteretic performance is used to calculate the maximum demand during a seismic event for the CIP, PCB1 and PCB2 bridge bents. Figure 5.12 shows the hysteretic performance during the FF19 and NF19 earthquakes.

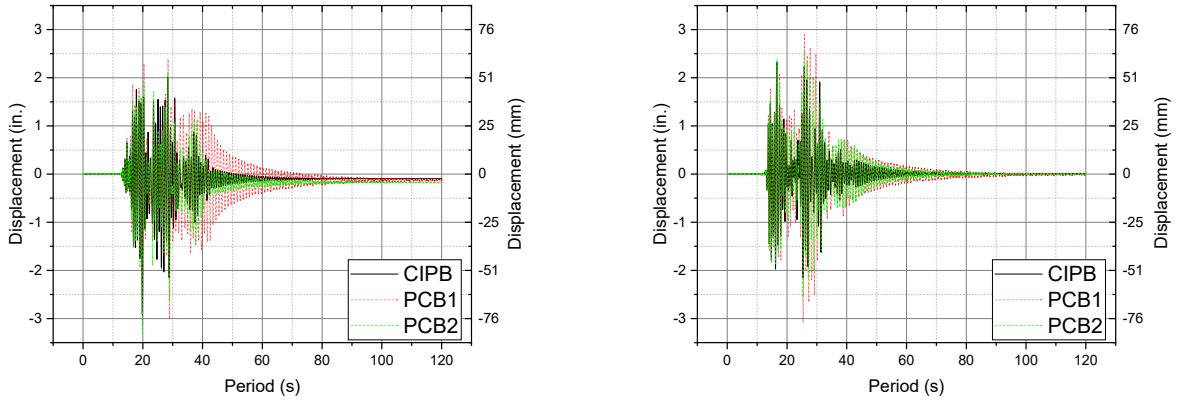


**Figure 5.11** Top node displacement: (a) FF19; and (b) NF12

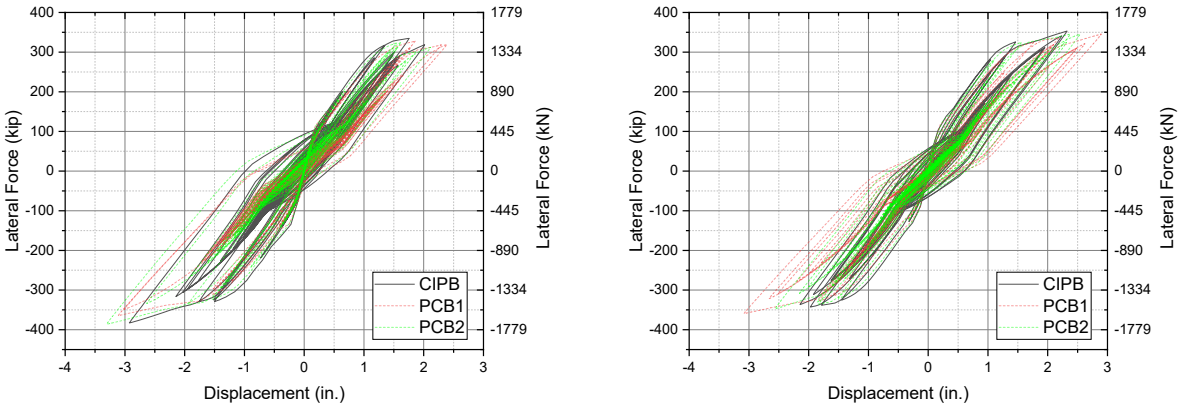


**Figure 5.12** Hysteretic performance of bridge bent: (a) FF19; and (b) NF12

After obtaining the TH and hysteretic plots for the DBE and MCE earthquakes for the three types of bridge bents, the response in terms of demand-to-capacity ratio was computed. This demand-to-capacity ratio would suggest which bridge bent had the better performing columns during a seismic event. Demand-to-capacity ratio is taken as a parameter to compare the performance of monolithic construction and precast construction with recessed spliced sleeves and intentional debonding. The demand-to-capacity representation showed that this ratio is less in terms of precast construction followed by monolithic construction for the case of the DBE. This lower value suggests that the capacity of the precast bent is higher than that of the monolithic bridge bent, suggesting better performance of the precast bent than that of the monolithic construction technique. This pattern also was followed for the scaled ground motion times 1.5 the original value, i.e., the MCE. Figure 5.13 shows the demand-to-capacity ratio for the DBE and MCE level for both the NF and FF earthquakes when the ultimate drift ratio is taken as the parameter for demand-to-capacity computation. Figure 5.14 shows the demand-to-capacity ratio for the DBE and MCE level for both the NF and FF earthquakes when the drift ratio at maximum lateral load is taken as the parameter for demand-to-capacity computation. The main idea of using recessed spliced sleeves and intentional debonding was to emulate the performance of monolithic construction; however, the use of recessed spliced sleeves and intentional debonding not only matched but also improved the performance.

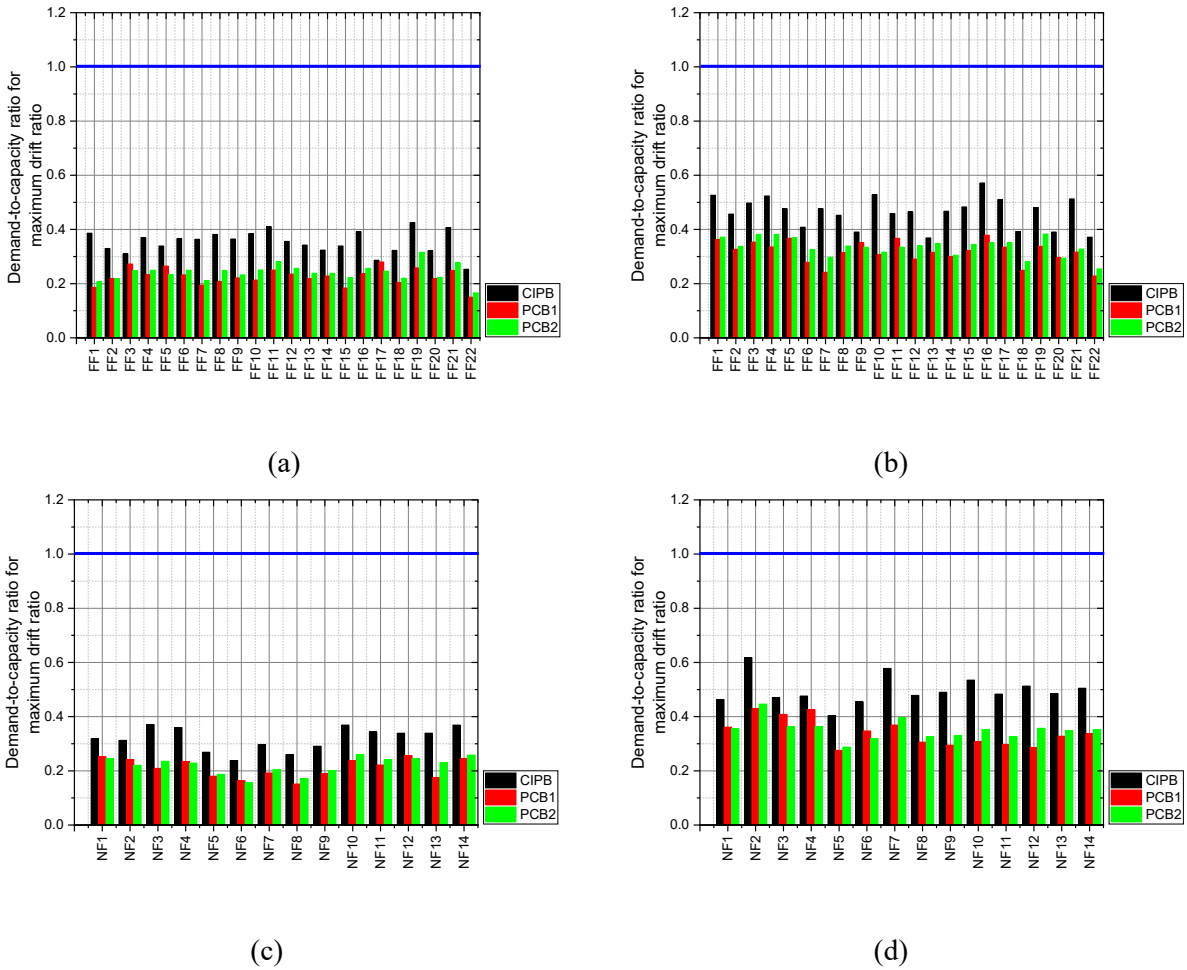


**Figure 5.13** Demand-to-capacity ratio for maximum drift ratio for bridge bent with new seismic details: (a) FF spectrally matched to DBE; (b) FF spectrally matched to DBE and scaled to MCE values; (c) NF spectrally matched to DBE; and (d) NF spectrally matched to DBE and scaled to MCE values

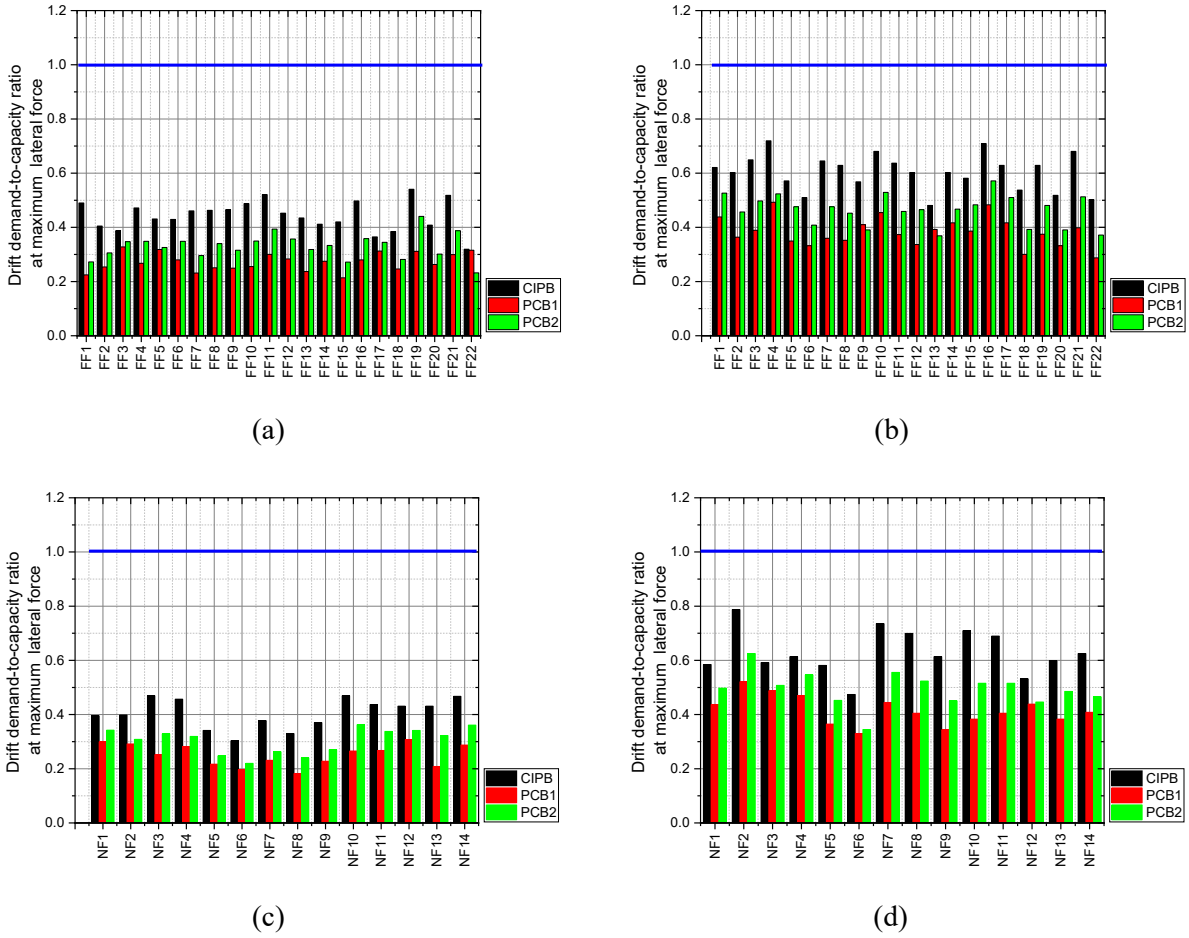


**Figure 5.14** Demand-to-capacity ratio for drift ratio at maximum lateral load for bridge bent with new seismic details: (a) FF spectrally matched to DBE, (b) FF spectrally matched to DBE and scaled to MCE values; (c) NF spectrally matched to DBE; and (d) NF spectrally matched to DBE and scaled to MCE values

# 6. DESIGN RECOMMENDATIONS

Based on the experimental study and numerical analysis of half-scaled bridge bents and an actual bridge bent, precast construction using the recessed splice sleeve details presented in this research can imitate the response of monolithic construction and even improve it. For a superior design of such a structure the following design recommendations are proposed:

- Use seismic design guidelines to design individual components of the precast structure.
- Precast structures can either be connected by recessed spliced sleeves or with grouted duct connections using the required length of embedment.
- If spliced sleeves are used, they should be recessed at least 8 bar diameters ($8d_b$) below the column-to-footing interface.
- The amount of intentional debonding heavily affects the performance; for a better response it is suggested to carry out intentional debonding inside the footing.
- The length of intentional debonding is preferred to be 8 bar diameters ($8d_b$).

# 7. SUMMARY AND CONCLUSIONS

## 7.1 Summary

This research was focused on establishing a numerical model that can emulate an experimental study performed on column-to-footing connections with recessed splice sleeve connectors (Barton et al. 2022). Once the numerical model was able to predict the behavior of the half-scaled specimens, a parametric study was carried out using the same precast details for an actual bridge bent. The numerical model included modeling of intentional debonding inside the footing, the column, or both the footing and the column. This numerical model also defines the bond-slip behavior, and the plastic hinge length required to estimate the actual seismic properties of the bridge bent. The numerical model could predict initial stiffness, maximum lateral load, peak displacement and the hysteretic energy of the experimental results. The loading and unloading curves matched quite well with the experimental result, suggesting there was adequate detailing in the numerical model. Results were compared at the global response and local response levels. Cumulative hysteretic energy, which is the global response parameter, had only a difference of 6% and 2% for the Test 1 and Test 2 type specimens, suggesting that the numerical model satisfied the criteria of global response. For the local response, reinforcing steel bar fracture was studied, and the cycle in which the bar fractured during the experiment was predicted perfectly by the numerical model, thus also verifying the criteria for local response.

Once the numerical model was able to predict the response, an actual bridge bent was modeled and the response was compared with experimental results for a three-column bridge bent, carried out by Pantelides et al. (2004). The numerical model showed good alignment with the experimental results; subsequently, monolithic and precast designs of the columns of the bridge bent were numerically modeled with different intentional debonding details. The proposed numerical model was then studied for the DBE and MCE level earthquakes for FF and NF type earthquakes. Demand-to-capacity ratio was computed for all three types of bridge bents. The demand-to-capacity response showed that precast bridge bents performed better than the monolithic bridge bent.

## 7.2 Conclusions

Based on the experimental and modeling results, the following conclusions are offered:

1. The numerical model proposed using *forceBeamColumn* element can predict the experimental results with recessed spliced sleeves with sufficient accuracy.
2. The numerical model includes bond-slip and intentional debonding effects. The numerical model proposed in this works well — and should be considered — in the analysis and design of bridge bents, including bond-slip and intentional debonding.
3. The effects of low-cycle fatigue and buckling of the reinforcing bars are essential in predicting accurate numerical results.
4. The technique, which includes considering the length of intentional debonding inside the footing to calculate the actual length of the plastic hinge, gives adequate numerical results.
5. Local and global response of the numerical model matched well with the experimental study, suggesting the numerical technique used to model cyclic behavior is satisfactory.
6. Parametric studies consisted of simulating an actual three-column bridge bent and using the numerical model to predict the seismic response including SSI; the results obtained using the numerical model agreed with the experiment in a satisfactory manner.
7. The capacity of the bridge bent was computed as a cyclic envelope rather than a pushover curve, which was used to compare the demand-to-capacity ratio during NF and FF ground motions.

8. The demand-to-capacity ratio implies that the precast bridge bents with recessed slice sleeves and intentional debonding perform better than a cast-in-place type of bridge bent, since they demonstrate a larger drift capacity.
9. Compared to monolithic type bridge bents, the findings of the experiments and the parametric research suggest that the use of complete or partial intentional debonding with recessed splice sleeves inside the footings of precast type bridge bents has significant advantages with respect to improved seismic performance.

## 7.3 Recommendations for Further Research

This research deals with the numerical model for predicting the behavior of column-to-footing joints when recessed spliced sleeves and intentional debonding are used inside the footings of bridge bents. The numerical model was validated for only two experiments; to ensure the accuracy of the numerical model in different situations, it is necessary to perform many experimental studies and validate them with the numerical model. Only one parametric study of the bridge bent was performed and presented; it is essential to perform experiments at actual full scale to confirm the accuracy of the numerical model. The computational model uses an equivalent circular column even though the tested columns had an octagonal cross section; OpenSees offers a more straightforward fiber discretization for circular sections. An automatic discretization of common concrete sections can produce a greater degree of accuracy, even if this has a small impact on the model's total response.

To further the current understanding of precast connections for bridge substructures using grouted splice sleeves, more experimental studies must be carried out. In addition to changes to the computational model and the constitutive laws, this involves further testing on large-scale subassemblies or tests of the connections utilizing enhanced grout mix designs under varied loading conditions.

# 8. REFERENCES


AASTHO. 2011. “AASTHO guide specifications for LRFD seismic bridge design.” *Transportation (Amst).*, (May): 1 v. (loose-leaf).

AASTHO. 2020. “AASTHO LRFD Bridge Design Specifications, 9th Edition - Table of Contents & Index.”

Ameli, M. J., D. N. Brown, J. E. Parks, and C. Pantelides. 2016. “Seismic Column-to-Footing Connections Using Grouted Splice Sleeves.” *ACI Struct. J.*, 113 (5). https://doi.org/10.14359/51688755.

Ameli, M. J., and C. P. Pantelides. 2017. “Seismic Analysis of Precast Concrete Bridge Columns Connected with Grouted Splice Sleeve Connectors.” *J. Struct. Eng.*, 143 (2): 04016176. https://doi.org/10.1061/(asce)st.1943-541x.0001678.

Ameli, M. J., J. E. Parks, D. N. Brown, and C. P. Pantelides. 2015. “Seismic evaluation of grouted splice sleeve connections for reinforced precast concrete column–to–cap beam joints in accelerated bridge construction.” *PCI J.*, 80–103.

Bartlett, S. F. 2004. “Ground response analysis and design spectra for UDOT bridges on soft soil sites.” *Draft Utah Dept. Transp. Rep., Dept. Civ. Environ. Eng. Univ. Utah, Salt Lake City*, 208.

Barton, R. D., M. J. Ameli, and C. P. Pantelides. 2022. “Precast Concrete Bridge Column-Footing Connections with Recessed Grouted Splice Sleeve Connectors.” *ACI Struct. J.*, (1).

Billington, S. L., and Yoon, J. K. (2004). “Cyclic Response of Unbonded Posttensioned Precast Columns with Ductile Fiber-Reinforced Concrete.” *Journal of Bridge Engineering*, 9(4), 353–363.

Bowman, B. W. (2016). “Modeling of Post-Tensioned Rocking Bridge Columns.” MS Thesis, University of Colorado, Boulder, CO.

Brenes, F. J., Wood, S. L., and Kreger, M. E. (2006). “Anchorage Requirements for Grouted Vertical-Duct Connectors in Precast Bent Cap Systems.” *Report No. FHWA/TX-06/0-4176-1*, Center for Transportation Research, University of Texas at Austin.

Dahal, P., M. Tazarv, and N. Wehbe. 2019. *Mechanical Bar Splices for Accelerated Construction of Bridge Columns Mechanical Bar Splices for Accelerated*.

Dangol, I., and C. P. Pantelides. 2022. “Resilient Posttensioned Bridge Bent with Buckling Restrained Brace.” *J. Bridg. Eng.*, 27 (2): 1–17. https://doi.org/10.1061/(asce)be.1943-5592.0001823.

Dangol, I., D. Thapa, and C. P. Pantelides. 2022. “Experimental evaluation of post-tensioned bridge bent under cyclic loads and comparison to hybrid bridge bents.” *Eng. Struct.*, 256 (December 2021): 113962. Elsevier Ltd. https://doi.org/10.1016/j.engstruct.2022.113962.

Dhakal, R. P., and K. Maekawa. 2002. “Modeling for Postyield Buckling of Reinforcement.” *J. Struct. Eng.*, 128 (9): 1139–1147. https://doi.org/10.1061/(asce)0733-9445(2002)128:9(1139).

Elsayed, W. M., M. A. N. Abdel Moaty, and M. E. Issa. 2016. “Effect of reinforcing steel debonding on RC frame performance in resisting progressive collapse.” *HBRC J.*, 12 (3): 242–254. Housing and Building National Research Center. https://doi.org/10.1016/j.hbrcj.2015.02.005.

Haber, Z. B. 2013. “Precast Column-Footing Connections for Accelerated Bridge Construction in Seismic Zones.” *Rep. No. CCEER 13-08; Cent. Civ. Eng. Earthq. Res. Dept. Civ. Environ. Eng. Univ. Nevada; Reno; NV*, (June): 661.

Haber, Z. B., M. Saiid Saiidi, and D. H. Sanders. 2015. “Behavior and simplified modeling of mechanical reinforcing bar splices.” *ACI Struct. J.*, 112 (2): 179–188. https://doi.org/10.14359/51687455.

Haber, Z. B., M. S. Saiidi, and D. H. Sanders. 2014. "Seismic performance of precast columns with mechanically spliced column-footing connections." *ACI Struct. J.*, 111 (3): 639–650. https://doi.org/10.14359/51686624.

Khaleghi, B., E. Schultz, S. Seguirant, L. Marsh, O. Haraldsson, M. Eberhard, and J. Stanton. 2012. "Accelerated bridge construction in Washington state: From research to practice." *PCI J.*, 57 (4): 34–49. https://doi.org/10.15554/pcij.09012012.34.49.

Kunnath, S. K., Y. Heo, and J. F. Mohle. 2009. "Nonlinear Uniaxial Material Model for Reinforcing Steel Bars." *J. Struct. Eng.*, 135 (4): 335–343. https://doi.org/10.1061/(asce)0733-9445(2009)135:4(335).

Kurama, Y. C., S. Sritharan, R. B. Fleischman, J. I. Restrepo, R. S. Henry, N. M. Cleland, S. K. Ghosh, and P. Bonelli. 2018. "Seismic-Resistant Precast Concrete Structures: State of the Art." *J. Struct. Eng.*, 144 (4): 03118001. https://doi.org/10.1061/(asce)st.1943-541x.0001972.

Mander, J. B., M. J. N. Priestley, and  and R. Park. 1988. "Theoretical Stress-Strain Model For Confined Concrete." *J. Struct. Eng.*, 114 (8): 1804–1826.

Manson, S. S. 1965. "Fatigue: a complex subject—some simple approximations." *Pap. Knowl. . Towar. a Media Hist. Doc.*

Mazzoni, S., F. McKenna, M. H. Scott, and G. L. Fenves. 2006. "Open System for Earthquake Engineering Simulation (OpenSEES) user command-language manual." *Pacific Earthq. Eng. Res. Cent.*, 465.

McKenna, F., Scott, M. H., and Fenves, G. L. (2010). "Nonlinear Finite-Element Analysis Software Architectire Using Object Composition." *Jounal of Computing in Civil Engineering*, 24(1), 95–107.

Melo, J., C. Fernandes, H. Varum, H. Rodrigues, A. Costa, and A. Arêde. 2011. "Numerical modelling of the cyclic behaviour of RC elements built with plain reinforcing bars." *Eng. Struct.*, 33 (2): 273–286. Elsevier Ltd. https://doi.org/10.1016/j.engstruct.2010.11.005.

Panagiotakos, T. B., and M. N. Fardis. 2001. "Deformations of Reinforced Concrete Members at Yielding and Ultimate." *Aci Struct. J.*, 98: 135–148.

Pang, J. B. K., M. O. Eberhard, and J. F. Stanton. 2010. "Large-Bar Connection for Precast Bridge Bents in Seismic Regions." *J. Bridg. Eng.*, 15 (3): 231–239. https://doi.org/10.1061/(asce)be.1943-5592.0000081.

Pantelides, C. P., J. P. Ward, and L. D. Reaveley. 2004. "Behavior of R/C Bridge Bent with Grade Beam Retrofit under Simulated Earthquake Loads." *Earthq. Spectra*, 20 (1): 91–118. https://doi.org/10.1193/1.1646163.

Priestley et al. 1996a. "Seismic design and retrofit of bridges, Wiley, New York." 1–21.

Priestley, M. J. N., F. Seible, and G. M. Calvi. 1996b. *Seismic design and retrofit of bridges*. John Wiley & Sons.

Raynor, D. J., Lehman, D. E., and Stanton, J. F. (2002). "Bond-slip response of reinforcing bars grouted in ducts." *ACI Structural Journal*, 99(5), 568–576.

Scott, M. H. 2007. "Numerical Integration Options for the Force-Based Beam-Column Element in OpenSees." *J. Intell. Mater. Syst. Struct.*, 18 (19): 1111-1120.

Sideris, P. 2012. "Seismic analysis and design of precast concrete segmental bridges." *ProQuest Diss. Theses*, 1100.

Tazarv, M., and M. S. Saiidi. 2014. “Next generation of bridge columns for accelerated bridge construction in high seismic zones.” (65): 1–19.

Tazarv, M., and M. S. Saiidi. 2015. “UHPC-filled duct connections for accelerated bridge construction of RC columns in high seismic zones.” *Eng. Struct.*, 99: 413–422. Elsevier Ltd. https://doi.org/10.1016/j.engstruct.2015.05.018.

Tazarv, M., and M. S. Saiidi. 2016. “Low-Damage Precast Columns for Accelerated Bridge Construction in High Seismic Zones.” *J. Bridg. Eng.*, 21 (3): 04015056. https://doi.org/10.1061/(asce)be.1943-5592.0000806.

Thapa, D., and C. P. Pantelides. 2021. “Self-Centering Bridge Bent with Stretch Length Anchors as a Tension-Only Hysteretic Hybrid System.” *J. Struct. Eng.*, 147 (10): 04021163. https://doi.org/10.1061/(asce)st.1943-541x.0003146.

Wu, R. Y., and C. P. Pantelides. 2019. “Seismic evaluation of repaired multi-column bridge bent using static and dynamic analysis.” *Constr. Build. Mater.*, 208: 792–807. Elsevier Ltd. https://doi.org/10.1016/j.conbuildmat.2019.03.027.

Zhao, J., and S. Sritharan. 2007. “Modeling of strain penetration effects in fiber-based analysis of reinforced concrete structures.” *ACI Struct. J.*, 104 (2): 133–141. https://doi.org/10.14359/18525.